# JCTC Journal of Chemical Theory and Computation

## Topological Characterization of the Electron Density Laplacian in Crystals. The Case of the Group IV Elements

A. Otero-de-la-Roza* and Víctor Luaña*

*Departamento de Química Física y Analítica, Facultad de Química, Universidad de Oviedo, 33006 Oviedo, Spain*

**Abstract:** We discuss the rigorous characterization of the electron density Laplacian of crystals in terms of its topological properties: critical points (CPs), zero flux surfaces, and accumulation and depletion basins. Comparison with the atomic shell structure is exploited to characterize the numerous core critical points so that the important effort is applied to the more significant valence structure. Efficient algorithms are adapted or newly developed for the main tasks of topological study: finding the critical points, determining the 1D and 2D bundles of $(3, -1)$ and $(3, +1)$ CPs, and integrating well-defined properties within the accumulation and depletion basins. As an application of the tools and concepts developed we perform a quantitative analysis of chemical bonding on group IV semiconductors, mainly devoted to the properties of the diamond phase but also including the main effects of allotropy influences on these elements. The topological analysis of the Laplacian provides a complementary and very different image than the topology of the electron density. Whereas the Laplacian graphs show a qualitative agreement with Lewis classical model, the basin population analysis excludes direct quantitative relationships with Lewis pair and octet rules. In addition to the expected core and valence basins, all group IV elements show very important interstitial basins, that accumulate a large number of electrons and dominate the compressibility behavior of the crystals.

## 1. Introduction

The Quantum Theory of Atoms in Molecules (QTAIM) has been in use for some three decades now to determine chemical bonding properties as true observables of the electron wave function.[1-8] QTAIM studies are mainly based on the topological analysis of the electron density, $\rho(\boldsymbol{r})$, particularly the characterization of its critical points ($\rho$-CP), and the integration of every kind of quantum observable within the attraction basin of atomic nuclei. Both, theoretical and experimental electron densities have been the subject of such scrutiny and, in fact, QTAIM is the mainstream technique for the experimental analysis of chemical bonding.[3,9]

The name Quantum Chemical Topology (QCT) has been proposed by Popelier[10-12] to include the growing collection of methods inspired in the seminal work of Bader.[1] Studies based on the topological analysis of $\rho$, $\nabla^2\rho$, the electron localizing function (ELF),[13] the source function,[14] the momentum density,[15] the electron pair density,[16] and many other similar properties would be included under the umbrella of QCT. Beyond sharing many common techniques and language, the development of QCT is becoming a revolutionary perspective in the old quest for the chemistry holey grail: obtaining every bit of information regarding chemical bonding that exists in the experimentally or computationally available part of the wave function, with no recourse to unfounded simplifications. In other words, providing a strict physical foundation to the chemical bonding.

The value of the Laplacian of the electron density, $\nabla^2\rho(\boldsymbol{r})$, on the $\rho$-CPs has been used to distinguish between shared- and closed-shell bonding cases.[17] The Laplacian has also been instrumental in characterizing hydrogen bonding,[18-21] predict sites of nucleophilic and electrophilic attack, as well

* To whom correspondence should be addressed E-mail: alberto@carbono.quimica.uniovi.es; victor@carbono.quimica.uniovi.es.

as the reactivity propension,[22] used to follow chemical reactions[23,24] and to distinguish between Lewis nucleophilic and acidic zones of a molecule,[25,26] to name just some of its most prominent roles.

The electron density Laplacian has also received a lot of recent attention from the community of developers of exchange and correlation functionals. Quantum Monte Carlo investigations on the strongly inhomogeneous electron gas,[27,28] later extended to small molecules[29] and crystals,[30] have shown that "the nonlocal contributions to [the exchange-correlation energy density] contain an energetically significant component, the magnitude, shape, and sign of which are controlled by the Laplacian of the electron density".[27]

Such an important role sharply contrast with the fact that only a very small number of articles have been devoted to the full topological characterization of the electron density Laplacian,[6,11,31−34] and none of them has examined condensed matter systems. The full topological characterization of a three-dimensional (3D) scalar field like $\nabla^2\rho(r)$ requires, in our opinion, being able to complete, at least, three different tasks: (1) localizing efficiently the critical points (L-CPs in this case); (2) tracing the 1D (*field lines*) and 2D (*interbasin surfaces*) regions that start or end on the first- and second-order saddle points; and (3) integrating local properties within the 3D basins of the Laplacian maxima and minima. Whereas the first capability is included in the AIMPAC package[35] since the eighties and from this on many other molecular topological codes, Popelier's MORPHY[36] (since the 2001 version) is the only code that currently offers the three capabilities.

This article is devoted to the complete characterization of the electron density Laplacian in solids. In the next section, we examine the meanings and usages that are associated to the Laplacian. Section 3 considers briefly the consequences of the cusps that the nonrelativistic electron density shows at the nuclear positions under the Born−Oppenheimer approximation. Section 4 reviews the atomic shell structure that markedly influences the Laplacian topology in molecules and solids. This analysis of the shell structure will prove determinant for the difficult task of finding and classifying the abundance of critical points that can be found. Section 5 introduces the algorithms that we have adapted or created to complete the full topological analysis of the Laplacian. The analysis and discussion of our results in a representative set of crystals is the subject of section 6. We have selected the group IV elements for the first application of the new techniques: the examination of the five, C−Pb, elements on the same diamond phase will let us determine the influence of the number of electron shells, whereas the characteristic allotropy of these elements provides a window to the effect of crystal geometry on the topological properties. The article ends with a discussion of the main outcomes of our analysis and the prospect of the possible role of the presented techniques on the Quantum Chemical Topology studies.

## 2. Meaning of the Laplacian of the Electron Density

The most immediate meaning of the Laplacian comes from the geometrical interpretation: $\nabla^2\rho(r)$ provides the local curvature of the electron density at $r$. Hence, if $\nabla^2\rho(r) < 0$, the electron density at $r$ is larger, on average, than in the differential region surrounding this point. In other words, the electron density is locally enhanced or accumulated at $r$. Similarly, the electron density is locally depleted at those points where $\nabla^2\rho(r) > 0$. This role is consequence of the Laplacian being the trace of the Hessian or curvature matrix: $H(r) = \nabla\otimes\nabla\rho(r)$. Accordingly, $\nabla^2\rho(r)$ represents the accumulated curvature of the three-dimensional neighborhood of $r$.

This geometrical role of the Laplacian is stressed in the following equation, included by James C. Maxwell[37] in his *Treatise on Electricity and Magnetism* (1873):

$$\rho(r_a) - \rho_{av}(r_a) = -\frac{\tau^2}{10}\nabla^2\rho(r_a) + \mathcal{O}(\tau^4) \quad (1)$$

where $\rho_{av}(r_a)$ represents the average value of the electron density for all the points within a sphere of radius $\tau$ centered on $r_a$, and $\mathcal{O}(\tau^4)$ is a small term of the order of $\tau^4$. This equation led Maxwell to propose calling $L(r) = -\nabla^2\rho(r)$ the *"concentration of $\rho$ at the point $r$, because it indicates the excess of the value of $\rho$ at that point over its mean value in the neighborhood of the point"*.[37]

The use of $L(r)$ instead of $\nabla^2\rho(r)$ has also been customary in the QTAIM literature at least since 1984.[38] Looking for a more intuitive comparison with the behavior of the density, maxima in $L(r)$ represent maximal concentration of density in a similar way to maxima in $\rho(r)$ that represent the maximal accumulation of electronic charge which are typical of nuclei. We will adhere to this tradition and our topological characterization will be referred from now on to $L(r)$ rather than to $\nabla^2\rho(r)$.

The importance of the Laplacian for the QTAIM theory is further evidenced by the fundamental relationships in which it appears. Of tantamount importance is the *local virial relationship*:[17,39,40]

$$\frac{\hbar^2}{4m}\nabla^2\rho(r) = \mathcal{V}(r) + 2\mathcal{G}(r) \quad (2)$$

where $\mathcal{G}(r)$ is the kinetic energy density and $\mathcal{V}(r)$ is the electronic potential energy density. $\mathcal{G}(r)$ is everywhere positive, and $\mathcal{V}(r)$ is everywhere negative, so the sign of $\nabla^2\rho(r)$ indicates which of the two contributions to the local virial theorem dominates at every point. Acidic regions, characterized by $\nabla^2\rho(r) > 0$ show a kinetic energy dominance, whereas regions of basic character, $\nabla^2\rho(r) < 0$, show the dominance of the electronic potential energy.

Requiring that the virial relationship holds in an arbitrary region $\Omega$ leads to the QTAIM characterization of atomic basins by bounding zero flux surfaces

$$\nabla\rho(r)\cdot n(r) = 0 \quad (3)$$

where $n(r)$ is the normal vector to the surface at $r$. When and only when $\Omega$ is defined in this way then

$$\int_\Omega \nabla^2\rho(r)dr = \oint_{S(\Omega)} \nabla\rho(r)\cdot n(r)dr = 0 \quad (4)$$

Electron Density Laplacian

*J. Chem. Theory Comput., Vol. 6, No. 12, 2010* **3763**

In a similar way, $\nabla^2\rho$ can be shown to be the connection between different, but equally grounded, forms of the kinetic energy density. For instance[1,41]

$$\mathscr{K}(\mathbf{r}) = \mathscr{G}(\mathbf{r}) - \frac{\hbar^2}{4m}\nabla^2\rho(\mathbf{r}) \tag{5}$$

where

$$\mathscr{K}(\mathbf{r}) = -\frac{\hbar^2}{4m}\{\nabla^2 + \nabla'^2\}\Gamma^{(1)}(\mathbf{r},\mathbf{r}')|_{\mathbf{r}'\to\mathbf{r}} \tag{6}$$

$$\mathscr{G}(\mathbf{r}) = \frac{\hbar^2}{2m}\{\nabla^2\cdot\nabla'\}\Gamma^{(1)}(\mathbf{r},\mathbf{r}')|_{\mathbf{r}'\to\mathbf{r}} \tag{7}$$

and $\Gamma^{(1)}(\mathbf{r},\mathbf{r}')$ is the nondiagonal one-electron density matrix. Only when $\Omega$ satisfies the zero flux condition $\mathscr{K}(\Omega) = \mathscr{G}(\Omega)$ and, in general, all the different forms of defining locally the kinetic energy density yield equivalent results.

The $\Omega$ regions defined in terms of the zero-flux surface condition constitute the electron density *basins* and represent the fundamental partition of the molecular and crystalline space according to the QTAIM theory. *Atomic attraction basins*, containing a single nuclear $\rho$-CP, and *minima repulsion basins*, containing a single cage $\rho$-CP, are two alternative partitions that exhaustively divide the crystal into nonoverlapping regions. Both are made, in fact, by joining appropriately *primary bundles*, mathematically defined as the space region made of the gradient lines joining together a particular nucleus with a particular cage $\rho$-CP.[42]

This partitioning of space is not exclusive of the electron density. Any differentiable $C^2$ scalar field provides a partition with similar topological properties, including $L(\mathbf{r})$. We define, for instance, the *accumulation basins* and the *depletion basins* as the regions bounded by zero flux surfaces of $\nabla L(\mathbf{r})$ and associated to maxima and minima of $L(\mathbf{r})$, respectively. The electron density, however, stands alone as the only partition that guarantees the correct behavior of all quantum mechanical operators on the local level. As a consequence, we will be able to integrate, within the $L(\mathbf{r})$ basins, local properties, like the volume and charge, but not such nonlocal properties as the kinetic energy.

## 3. Laplacian and Nuclear Cusps in the Electron Density

It is well-known that nonrelativistic Born−Oppenheimer electron densities exhibit a singularity or cusp at the fixed nuclear positions.[43] This is a consequence of the infinite asymptote of the Coulomb potential because of a fixed-point-like nucleus. This singularity, that would preclude the existence of derivatives, including $\nabla^2\rho(\mathbf{r})$, at the nuclear positions is usually discarded by assuming the mapping of a smooth function identical in value and properties to $\rho(\mathbf{r})$ except that the cusps are eliminated and substituted by some rounded shape.[1]

It should be noticed, however, that the cusps are removed if nuclei are modeled as small but finite-size particles, as it is routinely done in atomic[44] and solid-state relativistic calculations.[45,46] Cusps would also disappear if the electron

**Table 1.** Rank and Signature ($\mathbf{r}$, $\sigma$) of the Hessian Matrix Can Be Used to Classify the Different Types of Critical Points[a]

| ($\mathbf{r}$, $\sigma$) | type | name | abbrev. | AD | RD |
|---|---|---|---|---|---|
| (3, −3) | maximum | nucleus | NCP | 3D | 0D |
| (3, −1) | saddle-1 | bond | BCP | 2D | 1D |
| (3, +1) | saddle-2 | ring | RCP | 1D | 2D |
| (3, +3) | minimum | cage | CCP | 0D | 3D |
| (2, −2) | 2D-maximum | | | 2D | 0D |
| (2, +0) | 2D-saddle | | | 1D | 1D |
| (2, +2) | 2D-minimum | | | 0D | 2D |
| (1, −1) | 1D-maximum | | | 1D | 0D |
| (1, +1) | 1D-minimum | | | 0D | 1D |

*a* The common name and the usual abbreviation is indicated as the third and fourth column, respectively. AD and RD are the dimensions of the attraction and repulsion basins, respectively, created by the critical point.

density is the result of some statistical ensemble where the nuclear motion is taken into account.

## 4. Topological Structure of $L(\mathbf{r}) = -\nabla^2\rho(\mathbf{r})$ and the Atomic-like Shell Structure

$L(\mathbf{r})$ induces a complete partition of the space into distinct and complementary regions by means of the gradient vector field, $\nabla L(\mathbf{r})$, described in terms of the critical points, $\mathbf{r}_c$:

$$\nabla L(\mathbf{r}_c) = \mathbf{0} \tag{8}$$

which can be classified by the rank and signature of the Hessian matrix:

$$H(\mathbf{r}_c) = \nabla \otimes \nabla L(\mathbf{r}_c) \tag{9}$$

Table 1 gives a summary of the type and properties of the regular (i.e., 3D) and degenerated (2D or 1D) critical points of $L(\mathbf{r})$, and establishes the notation for the rest of the paper. We have decided to keep the same denominations already popular when describing the topology of $\rho(\mathbf{r})$. If confusion is possible, we will refer to $\rho$-CP or L-CP to distinguish between the critical points of both scalar fields.

Both, the electron density and the $L(\mathbf{r})$ scalar fields inherit their basic structure directly from the atoms. The electron density, peaked at the nuclear position, is formed by a collection of exponential arcs (one for each electronic shell, see Figure 1, left) connected by regions of larger curvature.

The shell structure is far more clearly revealed by the $L(\mathbf{r})$ function (see Figure 1, right). Starting from the nucleus, $L(\mathbf{r})$ shows a succession of maxima, zeros, minima, and zeros that we have labeled as $K_+$, KK, $K_-$ (for the 1s electrons), KL, $L_+$, LL, $L_-$ (the 2sp shell), LM, $M_+$, MM, $M_-$ (the 3spd shell), and so on. These features in the radial $L(\mathbf{r})$ function correspond to spheres of degenerate critical points in the 3D $L(\mathbf{r})$ field for the isolated atom. The spherical symmetry is broken by the influence of the neighbor atoms in a molecule or solid, but there is a neat difference between the effects shown by the core and valence shells. Whereas the internal shells keep unaltered the distance to the nucleus of their topological spots, the outermost shell loses to a large part its atomic origin and it is determined by the competition between the neighbor atoms, like it happens to the electron density itself.
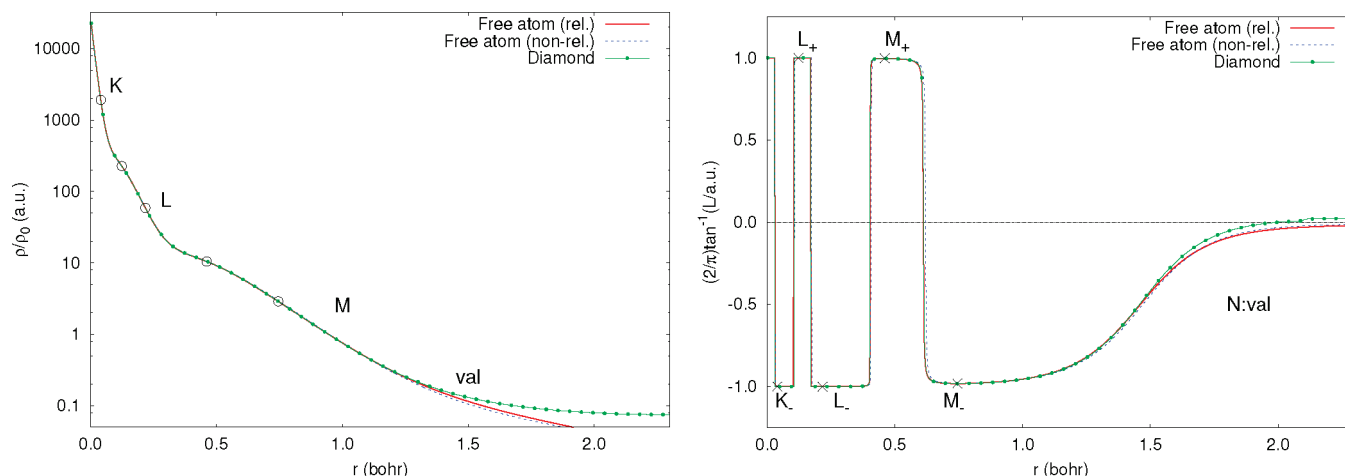
**Figure 1.** Radial structure of the electron density (left) and $L(\mathbf{r})$ (right) of Ge. The results from a nonrelativistic Hartree−Fock atomic calculation,[47] a relativistic Dirac−Fock atomic calculation,[44,48,49] and a relativistic FPLAPW calculation of the diamond phase of germanium are shown in both plots. The latter treats core states fully relativistically, while the scalar relativistic approximation is used for valence states.[49] The points $K_+$, $L_+$, are the maxima of $L(\mathbf{r})$ and $K_-$, $L−$, are the minima. Notice the log scale of the left plot. Similarly, an arctangent scale is used on the right plot, transforming the $(−∞, +∞)$ range of $L(\mathbf{r})$ into $[−1, 1]$, with a minimal distortion of the region close to zero, the most significative one from a chemical bonding perspective.

Figure 1 also shows that the core region experiences a negligible relative modification because of the environment, as well as the relativistic effects, both on $\rho(\mathbf{r})$ and $L(\mathbf{r})$. It is only the valence region that suffers the significant changes.

The association of the Laplacian of the electron density and the atomic shell structure was first formulated by Bader et al.[17,50] ref. 50 in particular, started the association of an electronic shell with a pair of spherical shells of alternating charge concentration and charge depletion, later accepted by most researchers. These initial studies, performed on light elements of the main groups, were later extended to heavier atoms by Sagar et al.,[51] Shi and Boyd,[52] and Kohout et al.[53] Those works have shown that, using Bader's definition, the Laplacian of $\rho$ fails sometimes to resolve the valence from the inner shells, a problem that starts to occur in some elements of the fourth row of the periodic table and becomes more common as we progress to heavier elements. This was a common argument for the introduction of the Electron Localization Function (ELF)[13] that shows similar properties to $L(r)$ but maintains the core−valence difference up to the sixth row, at least. Following Eickerling and Reiher,[54] authors of the most extensive analysis to date of the Laplacian of relativistic multiconfigurational atomic calculations, we consider that all topological features of $L(\mathbf{r})$ should be considered: maxima, minima, and zeros. For elements $Z > 18$, the assumed valence electronic shell is not observable as a local maximum in the positive region of $L(\mathbf{r})$, but the maximum remains even though in the negative region.

In any case, our main interest regarding the shell structure lies in the possibility of knowing in advance how a spherical shell will contribute to the topology of $L(r)$ in a molecule or crystal. This will help us in classifying and naming the large number of L-CPs that typically occur. The number and type of L-CPs in a unit cell is restricted by the Morse relationship,

$$n - b + r - c = 0 \qquad (10)$$

where $n$, $b$, $r$, and $c$ are the number of NCP, BCP, RCP, and CCP, respectively, per unit cell. The degeneracy of an atomic

spherical shell is broken by the potential of the neighbor atoms. In the case of core shells, the resulting L-CPs move negligibly in the radial direction, and the radial curvature of $L(r)$ also changes negligibly. Moreover, the L-CPs produced by the symmetry breaking of a core shell are topologically equivalent to a polyhedron and the Euler relationship must be fulfilled:

$$\text{vertices} - \text{edges} + \text{faces} = 2 \qquad (11)$$

When the core shell corresponds to a maximum of $L(\mathbf{r})$, the radial curvature is negative and the breaking of atomic symmetry can only produce NCP, BCP, and RCP, but not $(3, +3)$ points. In this case, NCPs are the vertices, the 1D repulsion basins of BCPs form the edges, and the 2D repulsion basins of RCP's are the faces of the polyhedron. Accordingly, the radial maximum in $L(\mathbf{r})$ produces

$$n_+ - b_+ + r_+ = +2 \qquad (12)$$

a contribution of $+2$ to the global Morse sum. Contrarily, a core minimum of $L(\mathbf{r})$, with a positive radial curvature, decomposes into CCPs (vertices), RCPs (edges), and BCPs (faces) but no NCPs. Their contribution to the Morse sum is, therefore

$$-b_- + r_- - c_- = -2 \qquad (13)$$

Table 2 shows the mean radii of the mostly spherical shells for C−Pb in their cubic diamond phase. The $K_+$ position is essentially coincident with the nucleus and it is considered to remain a single point, although the behavior of the electron density at the nucleus depends, on relativistic calculations, of the type of model used to describe the nuclear charge. From our point of view it is enough to consider that the unsplit $K_+$ point contributes $+1$ to the Morse sum. Each pair of successive minimum plus maximum radial shells compensate to produce a null net Morse contribution. A last, uncompensated radial minimum shell would change the global core contribution from $+1$ to $−1$. This is what happens

**Table 2.** Mean Radius of the Spherical Shell Diamond Structure[a]

|  | C | Si | Ge | Sn | Pb |  |
|---|---|---|---|---|---|---|
| K+ | 0 | 0 | 0 | 0 | 0 | K+ |
| KK | 0.16844 | 0.07018 | 0.02915 | 0.01729 | 0.00804 | KK |
| K− | 0.23042 | 0.09600 | 0.03992 | 0.02381 | 0.01134 | K− |
| KL | 0.84696 | 0.27785 | 0.10452 | 0.06248 | 0.03426 | KL |
| L+ | 0.98123 | 0.32665 | 0.12327 | 0.07362 | 0.04015 | L+ |
| LL |  | 0.47154 | 0.17100 | 0.10058 | 0.05363 | LL |
| L− |  | 0.59910 | 0.21708 | 0.12735 | 0.06825 | L− |
| LM |  | 1.59407 | 0.40355 | 0.21606 | 0.11223 | LM |
| M+ |  | 1.83266 | 0.46067 | 0.24758 | 0.12846 | M+ |
| MM |  |  | 0.61172 | 0.31794 | 0.16148 | MM |
| M− |  |  | 0.74538 | 0.38810 | 0.19615 | M− |
| MN |  |  | 2.03817 | 0.65597 | 0.29462 | MN |
| N+ |  |  |  | 0.73175 | 0.33214 | N+ |
| NN |  |  |  | 0.92299 | 0.41801 | NN |
| N− |  |  |  | 1.09627 | 0.49510 | N− |
| NO |  |  |  |  |  | NO |
| O+ |  |  |  |  | 0.96772 | O+ |
| OO |  |  |  |  |  | OO |
| O− |  |  |  |  | 1.11951 | O− |
| $R_{NN}/2$ | 1.45931 | 2.22190 | 2.31464 | 2.65579 | 2.88807 |  |

[a] The horizontal lines mark the end of the core shell structure.

in C, Si, Ge, and Pb, but not in Sn, according to Table 2. Anyway, the consideration of what constitutes a core and what a valence shell depends upon the criterion used to accept that two Laplacian critical points have the same distance relative to the nucleus.

Our description in this section is not specific of the $L(\mathbf{r})$ function, but it can be applied to any scalar field showing an atomic shell structure. The ELF function comes immediately to mind, but many other similar fields can also be included.

## 5. Implementing the Topological Analysis of the Electron Density Laplacian in Crystals

The rich literature exploring the topology and properties of the Laplacian in molecules or for light elements has been discussed in previous sections. However, to the best of our knowledge, this is the first article devoted to the full topology of $L(\mathbf{r})$ in crystals and addressing solids with arbitrarily heavy elements. The reason behind this apparent neglect rests in the extreme behavior of the $L(\mathbf{r})$ scalar function. In this section, we describe the important modifications and new techniques that must be introduced in the usual QCT algorithms when analyzing $L(\mathbf{r})$. The principles and methods that will be described can be readily generalized to other scalar fields showing atomic shell structure, such as the ELF,[13,55] and the noninteracting electron pressure,[56] for instance.

As described previously, $L(\mathbf{r})$ displays a shell structure around the atoms: there exist regions surrounding the nuclei that present large value fluctuations, specially near the nucleus. If the atom were isolated, $L(\mathbf{r})$ would have a strict spherical symmetry. After the formation of the crystal, $L(\mathbf{r})$ is distorted, acquiring the symmetry of the local point group. However, the shell structure is maintained and the distortion is small, specially in the core region. The heavier elements show the sharpest oscillations. As an example, the value of $L(\mathbf{r})$ in the Pb atom varies more up to 14 orders of magnitude

between the $K_+$ ($L \approx 10^8$) and $L_-$ ($L \approx -10^6$) radial extrema. This example shows clearly the necessity for specialized algorithms to deal with shell-structured scalar fields.

The topological characterization of a scalar field $f(\mathbf{r})$, rests on three main tasks: the integration of the trajectories of $\nabla f$, the localization of all the critical points of $f$, and the integration of properties on the attractor basins. The computational bottleneck is the latter by far.

Starting with the seminal work by Biegler-König,[57,58] a number of methods have been developed to deal with the problem of locating the interattractor surface (IAS) and integrating the property densities.[34,59−62] Most of them, however, are density-specific and not suitable for generic scalar fields, where the basins have different shapes[11] and geometrical properties. In the case of light molecules, Popelier has successfully applied a collection of strategies, including a specialized octree algorithm,[34] to the calculation of the basin properties of $L(\mathbf{r})$.

In this work, we have preferred to adopt the old and simple but robust bisection technique. Several reasons have lead us to use it: (a) the algorithm is general enough to deal with any basin shape, provided there are no multiple crossings of the ray and the IAS, and even that can be taken into account; (b) it is reasonably efficient if the gradient paths are traced sensibly (see below); and (c) it allows arbitrary precision of integration by increasing the number of rays, with an error given by the cubature employed and the precision of the IAS. Bisection depends on the efficiency of the gradient path tracing, and its performance is independent of the scalar field, so the three above-mentioned tasks of the QCT study reduce to two core routines: tracing gradient paths and finding the whole set of critical points.

**5.1. Source of the $L(\mathbf{r})$ Function.** First, let us examine the technical details of the analysis of $L(\mathbf{r})$ in solids. The $L(\mathbf{r})$ field is a quantum-mechanical observable, and as such, its features and the insights gained from its analysis are independent of the method used in its determination. In practice, however, both theory and experiments have shortcomings and the $L(\mathbf{r})$ field is obtained only as an approximation, and is subject to the limitations of the determination method.

Our approach to $L(\mathbf{r})$ in this article is based on the full-potential (linearized) augmented plane-waves method (FPLAPW)[63,64] as implemented in wien2k.[45,46] In the FPLAPW method, the real space is partitioned into regions, roughly corresponding to the core and valence zones of the solid. These regions are: the muffin tins, noncolliding spheres centered around each atom, and the interstitial space, that fills the rest of the crystal. The basis functions (APW or LAPW) and the density are split, behaving differently in each region. In particular, the density is expressed as

$$\rho(\mathbf{r}) = \begin{cases} \sum_{LM} \rho_{LM}(r) Y_L^M(\hat{r}) & \mathbf{r} \in S_\alpha \\ \sum_K \rho_K e^{i\mathbf{K}\mathbf{r}} & \mathbf{r} \in 1 \end{cases} \quad (14)$$

In the muffin tin of the $\alpha$ nucleus ($S_\alpha$), with radius $R_{mt}$, the density is expressed as a spherical harmonics ($Y_L^M$) expansion referred to its corresponding center (the position of the

nucleus), while in the interstitial region (*I*), $\rho$ is written as a plane-wave expansion, where $K$ is a reciprocal lattice vector. The Laplacian of the density has a similar form

$$\nabla^2\rho(r) = \begin{cases} \sum_{LM} f_{LM}(r)Y_L^M(\hat{r}) & r \in S_\alpha \\ -\sum_K K^2\rho_K e^{iKr} & r \in 1 \end{cases} \quad (15)$$

with

$$f_{LM}(r) = \rho''_{LM} + \frac{2}{r}\rho'_{LM} - \frac{L(L+1)}{r^2}\rho_{LM} \quad (16)$$

where primes represent differentiation in the radial coordinate. In both expressions, the expansion is carried not to the infinite set of local spherical harmonics and plane waves, but it is included only up to certain cutoff values $L_{max}$ and $K_{max}$. This truncation creates discontinuous gaps on the muffin tin surface that need to be dealt with by the topological algorithms. The absence of continuity in $\rho(r)$ and $L(r)$ is thus a basic, inescapable feature of the FPLAPW densities.

How does the lack of continuity at the muffin tin surface affect the results of the analysis? We have found that the discontinuity is invisible to both the CP localization method and to the gradient path tracer, provided there are no spurious critical points on the muffin tin surface. This applies for both the density and its Laplacian. The spurious CPs trap gradient path integrations in an anomalous way and, being the consequence of a discontinuous gap, their number do not fulfill the Morse sum criterion. Tuning of the calculation parameters seems to be the only way around the problem, being most sensitive to the variation of $R_{mt}K_{max}$ and $R_{mt}$. A very large value of $L_{max}$ could, in principle, be effective but it is not possible to go beyond a hard-coded 10 value without a severe reprogramming of many parts of the wien2k[45,46] code.

There is a further consequence of the discontinuity that must be taken into account. The discontinuity introduces a surface term in the integral of $L(r)$ over the unit cell. Using Gauss theorem, it can be expressed as a flux of the density gradient across the muffin surfaces:

$$\int_{cell} L(r)dr = -\sum_\alpha \oint_{S_\alpha} (\nabla\rho_\alpha - \nabla\rho_i) \cdot dS \quad (17)$$

where $\alpha$ runs over the atoms in the cell, $\rho_i$ and $\rho_\alpha$ are the density function forms in the interstitial, and the $\alpha$ muffin (eq 14), respectively. This result has two important consequences: the $\mathscr{G}$ and $\mathscr{K}$ forms of the kinetic energy are not equivalent, the one entering the total energy expression being $\mathscr{G}$[65,66] and the integral of $L(r)$ within the topological ($\nabla\rho$) basins is not zero. Note that, although the sum in eq 17 can be easily computed to correct the integral of $L$ over the cell, it is not possible to do the same to the atomic expectation values of $L$, except in the cases where no muffin crosses the interatomic surface.

To test our algorithms, we have selected a set of systems, containing an assortment of bonding characters and structures. These are listed in Table 3, along with their main

**Table 3.** Test Cases for the Evaluation of the Algorithms Related to the Analysis of $L(r)^a$

| crystal | phase | $R_{mt}K_{max}$ | k-points (1BZ) | $R_{mt},1$ | $R_{mt},2$ |
|---------|-------|-----------------|----------------|------------|------------|
| AlN | blende | 9.0 | 1000 | 1.77 | 1.30 |
| AlN | wurzite | 9.0 | 1000 | 1.77 | 1.30 |
| AlP | blende | 9.0 | 4000 | 1.50 | 2.10 |
| BN | blende | 10.0 | 1000 | 1.45 | 1.20 |
| BP | blende | 10.0 | 2000 | 1.59 | 2.00 |
| C | graphite | 9.0 | 60000 | 1.20 | |
| C | diamond | 9.0 | 60000 | 1.30 | |
| GaN | blende | 9.0 | 1000 | 1.70 | 1.40 |
| GaN | wurzite | 9.0 | 1000 | 1.70 | 1.40 |
| GaP | blende | 11.0 | 1000 | 2.00 | 2.00 |
| Ge | diamond | 11.0 | 8000 | 2.21 | |
| Li | BCC | 9.0 | 60000 | 2.20 | |
| Mg | HCP | 9.0 | 60000 | 2.90 | |
| NaCl | rock salt | 9.0 | 60000 | 2.30 | 2.30 |
| Na | BCC | 9.0 | 60000 | 2.20 | |
| Pb | diamond | 10.0 | 60000 | 2.30 | |
| Pb | FCC | 10.0 | 60000 | 2.30 | |
| Si | diamond | 11.0 | 8000 | 2.21 | |
| Sn | diamond | 10.0 | 8000 | 2.30 | |
| Sn | tetragonal | 10.0 | 14000 | 2.60 | |

*a* All the geometries correspond to the experimental structures,[70,71] with the exception of the diamond phase of Pb, that was optimized using FPLAPW and a Perdew−Burke−Erzenhof exchange-correlation functional, to a cell parameter of *a* = 13.339 bohr.

calculation conditions. The number of *k*-points in the full first Brillouin zone (1BZ) was chosen so that the energy converged to the precision of the code in all the crystals but the metallic (Li, Mg, Na, Pb, and Sn). The FPLAPW calculations have been done using the Perdew−Burke−Ernzerhof[67] GGA functional. We have used the runwien text interface[68] to wien2k to carry out the calculations and a modified version of critic[69] to perform the QTAIM analysis.

All the crystals in the Table 3 have been examined for the existence of spurious CPs by means of a direct and simple test: a number of $n_\theta \times n_\phi$ points are uniformly distributed in spheres of radii $R_{mt} - \varepsilon$ and $R_{mt} + \varepsilon$ around each atom, with $\varepsilon = 10^{-3}$ bohr. Consequently, one of the spheres is inside the muffin tin and the other is in the interstitial region. Every point in the inner sphere has a counterpart in the other one, at a distance $2\varepsilon$. The radial component of the gradient of the scalar field, $f_r$, is then computed at each pair of points. Spurious CPs exist whenever a pair of points differ in the sign of their $f_r$. The calculation conditions were then modified for each crystal until some combination produced a density and Laplacian free from discontinuities on all tested directions. This extense exploration of calculation parameters has revealed that, in these systems, the occurrence of spurious CPs does not depend on the number of *k*-points, but it is affected heavily by the values of $R_{mt}K_{max}$ and $R_{mt}$. In most cases, the electron density was correct under a wide range of calculation conditions and it was the Laplacian the function posing real difficulties to the QTAIM analysis. The process of finding good parameters for III−V elements was specially painstaking, as no pattern for the occurrence of trouble was apparent.

**5.2. Navigation in the L(r) Surface.** Now, we describe the computational details of the analysis of $L(r)$. The first step is the computation of the shell structure of the scalar

Electron Density Laplacian

*J. Chem. Theory Comput., Vol. 6, No. 12, 2010* **3767**

field around each atom. On bonding, the inner shells of $L(r)$ are largely unaffected, while the valence shells are distorted to accommodate the environment. The position of the radial maxima and minima are determined by bracketing and golden section search in a number of rays emerging from the nucleus and uniformly distributed. The resulting shells are classified into: (a) valence shells, distorted by the chemical environment and possibly not fulfilling the shell Euler sum, and (b) core shells, resembling the atomic shells and fully closed. The innermost core shells do not convey any chemical information and are the most difficult to treat from the point of view of the algorithms. Therefore, for the heavier elements, we define an effective nucleus, that is composed of the real nucleus and a number of shells up to, and including, a $X_-$ shell, where $X = K, L, ....$ The structure within this effective nucleus is ignored by the algorithms, except that their actual contribution to the Morse sum is taken into account. The election of a shell that is a radial minimum as the frontier makes the effective nucleus a basin of $L(r)$, easy to integrate as a sphere.

The localization of the critical points of $L(r)$ is based on the Newton−Raphson (NR) method with two modifications to take into account the shell structure of $L(r)$. First, the same seeding scheme as in the electron density is used.[42,69] Namely, the irreducible wedge of the WS cell (IWS) is built by applying the local symmetry of the origin to the full WS cell. The IWS is split into disjoint tetrahedra and each of them undergoes a barycentric subdivision process to determine the starting points for the NR exploration. This method allows the rapid localization of the symmetry-forced CPs of $L(r)$. This scheme is inherently suited for solids, and far superior in efficiency to its molecular counterparts based on the search between pairs, triplets and quartets of atoms. In this particular scalar field, this strategy allows the localization of all the valence CPs, but requires high subdivision levels to locate the shell CPs. Therefore, we have added a new set of seed points, placed at the spherical shells of each atom, so as to locate the in-shell CPs.

The second necessary modification to NR consists of switching to spherical coordinates near the nuclei, at distances lower than the largest core shell. When the NR sequence of points falls into one of the inner shells, the transformation to spherical coordinates effectively decouples the radial from the in-shell (angular) coordinates. The Hessian matrix is thus approximately blocked. Special care must be taken regarding the numerical errors in the computation of the elements of the gradient ($f_i$, $i = r, \theta, \phi$) and the Hessian ($f_{ij}$, $i, j = r, \theta, \phi$). The radial components ($f_r$ and $f_{rr}$) are much larger than the ones involving the angular coordinates, so that the transformation of derivatives from Cartesian ($x_k$ values) to spherical ($s_i$) coordinates:

$$\frac{\partial}{\partial s_i} = \sum_k \frac{\partial}{\partial x_k} \frac{\partial x_k}{\partial s_i} \tag{18}$$

$$\frac{\partial^2}{\partial s_i \partial s_j} = \sum_k \frac{\partial}{\partial x_k} \frac{\partial^2 x_k}{\partial s_i \partial s_j} + \sum_{kl} \frac{\partial^2}{\partial x_k \partial x_l} \left(\frac{\partial x_l}{\partial s_i}\right)\left(\frac{\partial x_k}{\partial s_j}\right) \tag{19}$$

is subject to cancellation errors. In FPLAPW densities, a workaround to this problem is calculating the nonradial terms

**Table 4.** Summary of the Analysis of $L(r)$ in the Test Cases[a]

| crystal | phase | $L(r)$ topology | $t_{top}$ (s) |
|---|---|---|---|
| AlN | blende | 4(52)\|6(152)\|6(144)\|5(44) | 32.0 |
| AlN | wurzite | 7(26)\|13(76)\|14(74)\|8(24) | 97.1 |
| AlP | blende | 5(56)\|8(192)\|8(192)\|5(56) | 31.4 |
| BN | blende | 3(48)\|6(128)\|7(128)\|6(48) | 15.6 |
| BP | blende | 6(92)\|8(216)\|8(184)\|6(60) | 19.7 |
| C | graphite | 4(20)\|10(70)\|10(70)\|5(20) | 29.5 |
| C | diamond | 2(64)\|4(224)\|5(208)\|3(48) | 9.7 |
| GaN | blende | 4(52)\|6(152)\|6(144)\|5(44) | 25.3 |
| GaN | wurtzite | 7(26)\|14(78)\|13(72)\|6(20) | 90.7 |
| GaP | blende | 5(56)\|7(168)\|7(168)\|5(56) | 16.0 |
| Ge | diamond | 2(40)\|3(176)\|4(192)\|3(56) | 10.6 |
| Li | BCC | 2(28)\|4(120)\|4(114)\|3(22) | 3.6 |
| Mg | HCP | 4(14)\|8(56)\|7(58)\|3(16) | 2.5 |
| NaCl | rock salt | 4(64)\|6(200)\|5(200)\|3(64) | 5.6 |
| Na | BCC | 2(14)\|6(78)\|4(112)\|1(48) | 6.4 |
| Pb | diamond | 2(40)\|3(96)\|3(96)\|2(40) | 15.4 |
| Pb | FCC | 2(28)\|3(96)\|3(112)\|3(44) | 4.0 |
| Si | diamond | 4(168)\|6(352)\|6(256)\|3(72) | 11.6 |
| Sn | diamond | 2(40)\|3(176)\|4(192)\|3(56) | 15.8 |
| Sn | tetragonal | 2(20)\|6(80)\|7(104)\|4(44) | 19.8 |

[a] The full topology of $L(r)$ is shown in $n|b|r|c$ format. Each of these fields is of the form $x(y)$ where $x$ and $y$ are the number of CPs in the asymmetric and conventional unit cells respectively. All the topologies fulfill the global and shell Morse sum conditions. The cpu times correspond to a typical desktop PC. The computational cost increases in lower symmetry systems (e.g., wurtzite) because more NR search seeds are used.[69]

of the gradient and Hessian in the muffin tin by using an expression of $L(r)$ where the spherical term $L = 0$, $M = 0$ has not been summed. This eliminates the dominant spherical contribution to the value of $L(r)$ and prevents the cancellation errors in the transformation to spherical coordinates.

Additionally, a modified stop criterion for NR is necessary in the shells. Usually, a CP is located whenever $|\nabla f(r)| < \varepsilon$ where $\varepsilon$ is customarily set to $1 \times 10$. However, it is too difficult to find a radial component of the gradient below that threshold, because of the rapidly oscillatory character of $L(r)$ in the core region. Therefore, when in core shells, the norm of the gradient is calculated using only the angular coordinates.

The topologies of the test cases have been determined with the modified NR method. All the CPs of $L(r)$ have been located in less than two minutes on a typical desktop PC (see Table 4). The topologies fulfill the global and shell Morse conditions. If smaller effective nuclei are considered, the success of the modified NR algorithm in the innermost shells varies with the atom involved. For example, all the CPs of Ge are located, even if the effective nucleus is shrunk to only one shell, but this is not possible for chlorine (both in NaCl and in $Cl_2$), for which the $K_-$, $L_+$, and $L_-$ shells do not fulfill the local Morse sum using the default parameters of our modified NR. Popelier[32] and Gatti[72] have published finding the full topology of $L(r)$ by using the eigenvector-following method,[73] which we have also implemented using a transformation to spherical coordinates in core shells, as described above. By comparing to our modified NR method, we have found that eigenvector-following does not improve on the results of our method in terms of efficiency or success in locating CPs of $L(r)$, so we have opted for the simpler NR approach.

**5.3. Integration on the $L(r)$ Basins.** The other fundamental task in the analysis of $L(r)$ is the integration of gradient paths (GP). The basin integration method that we have chosen is bisection so the purpose of tracing of gradient trajectories boils down to two tasks: (a) locating the terminal points of the paths originating at a given gradient source and (b) depicting the behavior of the gradient vector field. In both of them, the primary concern is not the extreme accuracy of the paths but the computational efficiency, for GP tracing is the bottleneck of the integration of atomic properties. Consequently, we have chosen a simple explicit Euler method and included some modifications, similar to those introduced in the NR method, to provide for the special shell structure of $L(r)$.

As in NR, the integration of the GPs near the nuclei is done in spherical coordinates. For sufficiently inner shells, the adaptive step shrinks to the point of making the navigation impracticable, even with high order one-step methods. To avoid this problem, we have eliminated the radial coordinate from the GP tracing algorithm, provided several conditions are met: (a) the trajectory is traversing one of the known shells, (b) the shell has the correct curvature ($f_{rr} > 0$ if the trajectory goes downward, $f_{rr} < 0$ if upward), (c) the step size is smaller than $10^{-3}$ bohr, and (d) the absolute value of the radial curvature ($f_{rr}$) is greater than a certain value (in the $L(r)$ scalar field, this value is 1 au). For safety, the radial coordinate is optimized whenever the Newton-like step $|f_r/f_{rr}|$ is greater than $10^{-3}$ bohr. For core shells, this is seldom the case, as they remain approximately spherical on bonding. The radial coordinates are considered again whenever one of the above conditions, except (c), is not met, thereby taking into account the possibility of partial shells of $L(r)$.

If only the ending critical points of the GPs are needed, we have found that the use of $\beta$-spheres (the *atomic trust spheres*[74]) accelerates the assignment of the terminal atom by 4−6 times. The $\beta$-spheres are centered around each atom, with their radii being initially set to 75% of the distance of the atom to its closest bond critical point. The election of this radii follows from the ready availability of the complete list of CPs. When a GP enters a $\beta$-sphere, the terminal atom is automatically assigned to the owner of the sphere. This method prevents the expensive tracing of the gradient path near the nucleus, where the step size shrinks to prevent the gradient path from bouncing around the critical point. The case where one of the IAS retraces into one of the $\beta$-spheres is rare but possible, and a clear indication of this situation is the basin limit being assigned incorrectly to the surface of a $\beta$-sphere. Should this happen, the $\beta$-sphere radius is decreased by a factor and the basin limit is recalculated. We have checked that, in all the systems we examined, the value of the integrated atomic properties is not affected by the use of $\beta$-spheres.

## 6. Topological Analysis of Group IV Allotropes

As a first application of the newly developed topological tools we are going to analyze the diamond phase of the group IV elements: from C to Pb. We will also examine, as a term of

**Table 5.** wien2k Calculation Parameters Used for the Topological Analysis

| crystal | KPTS | RKMAX | RMT |
|---|---|---|---|
| C | 60000 | 9.0 | 1.30 |
| C (graphite) | 60000 | 9.0 | 1.20 |
| Si | 8000 | 11.0 | 2.21 |
| Ge | 5000 | 11.0 | 2.10 |
| Sn | 8000 | 10.0 | 2.30 |
| Sn (white) | 14000 | 10.0 | 2.60 |
| Pb | 60000 | 10.0 | 2.70 |
| Pb (fcc) | 60000 | 10.0 | 2.30 |

**Table 6.** Calculated (First Row) and Experimental (Second Row) Equilibrium Properties

| crystal | $a$ (Å) | $c$ (Å) | $B$ (GPa) |
|---|---|---|---|
| C | 3.5827 | | 444.3 |
| | 3.568 | | 444.0 |
| Si | 5.4797 | | 91.2 |
| | 5.4307 | | 99.2 |
| Ge | 5.5934 | | 75.1 |
| | 5.6574 | | 77 |
| Sn | 6.6563 | | 49.1 |
| | 6.49 | | 53 |
| Pb | 7.0589 | | 28.7 |
| Sn (white) | 5.9213 | 3.2280 | 63.7 |
| | 5.8197 | 3.1749 | 57.9 |
| Pb (fcc) | 5.0550 | | 36.0 |
| | 4.9502 | | 43.2 |

comparison, some allotropes that compete in stability with the diamond phase or are even the most stable phase under normal pressure and temperature: the graphite phase of C, the white or $\beta$-Sn, and the fcc or $\alpha$-Pb.

**6.1. Electronic Structure Calculations.** The electronic structure of all the crystals has been obtained from FPLAPW calculations using the wien2k[45,46] code with the new runwien text interface.[68] All calculations have been done using the Perdew-Burke-Ernzerhof[67] exchange and correlation functional. Care has been taken to converge the calculations with respect to all relevant internal parameters, in particular the muffin tin radius (RMT), the number of planewaves used as basis set (controlled by RKMAX), and the grid used to integrate the first Brillouin zone (controlled by KPTS). Table 5 shows the value of these essential parameters used in our calculations. It is important to notice that our requirements are somewhat different from those of a typical wien2k calculation. In most cases the FPLAPW codes are run using a muffin tin zone as large as possible to diminish the computational effort. In our case, we have to play carefully with the parameters to avoid, as much as possible, the discontinuity of the electron density and its derivatives at the muffin boundaries.

We have determined the equilibrium properties of the crystals, as a check of the calculations, and the most relevant results are collected in Table 6. In general, the equilibrium cell lengths are obtained within 1−2% of the experimental values, and the bulk moduli within 3% for the light elements and 10% for Sn and Pb. We have not included the graphite equilibrium geometry as it is well-known that typical GGA functionals are defective in their representation of intermolecular interactions and the graphene sheets are too loosely bound.

Electron Density Laplacian

*J. Chem. Theory Comput., Vol. 6, No. 12, 2010* **3769**
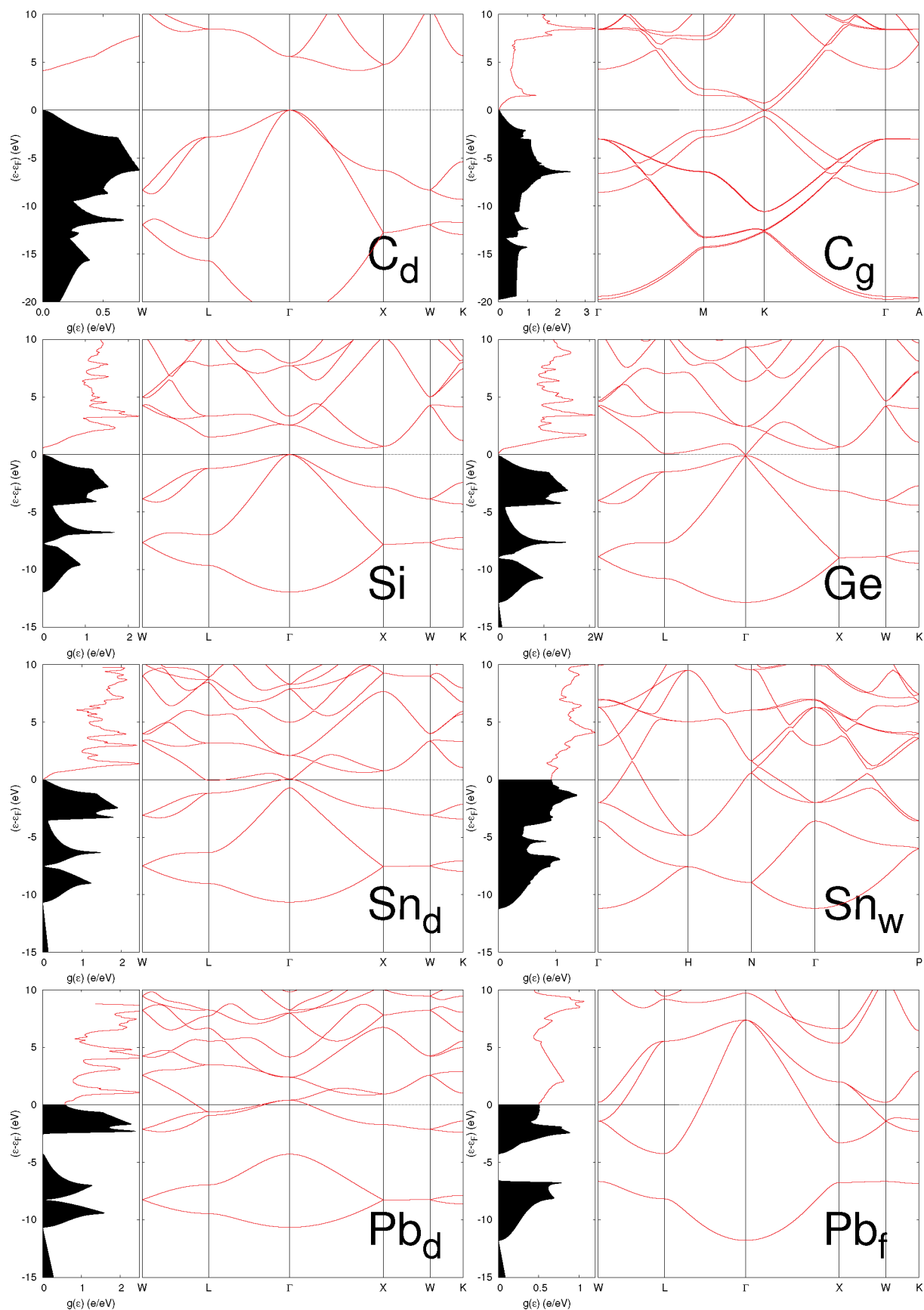


**Figure 2.** Band structure and density of states (DOS) for the diamond phases of C−Pb, graphite C, white Sn, and fcc Pb. The wien2k GGA calculations correspond to the experimental geometry, when available, and to the predicted equilibrium geometry otherwise.

C and Si are predicted to be semiconductors in the diamond phase, with an indirect band gap of 4.13 and 0.58

eV, respectively. These band gaps are significantly smaller than the experimental values of 5.5 and 1.1 eV, following

**Table 7.** Topology of the Electron Density for the Diamond Structures[a]

| CP | Wyckoff | position | $\rho(r_c)$ | $\nabla^2\rho(r_c)$ |
|---|---|---|---|---|
| C | *8a* | (1/8, 1/8, 1/8) | $1.28217 \times 10^2$ | |
| b | *16c* | (0, 0, 0) | 0.24005 | −0.55144 |
| r | *16d* | (1/2, 1/2, 1/2) | 0.21507 | +0.10522 |
| c | *8b* | (3/8, 3/8, 3/8) | 0.01323 | +0.07595 |
| Si | *8a* | (1/8, 1/8, 1/8) | $1.89360 \times 10^3$ | |
| b | *16c* | (0, 0, 0) | 0.08369 | −0.12344 |
| r | *16d* | (1/2, 1/2, 1/2) | 0.00559 | +0.01353 |
| c | *8b* | (3/8, 3/8, 3/8) | 0.00324 | +0.00897 |
| Ge | *8a* | (1/8, 1/8, 1/8) | $3.12582 \times 10^4$ | |
| b | *16c* | (0, 0, 0) | 0.07502 | −0.03556 |
| r | *16d* | (1/2, 1/2, 1/2) | 0.00436 | +0.01021 |
| c | *8b* | (3/8, 3/8, 3/8) | 0.00257 | +0.00652 |
| Sn | *8a* | (1/8, 1/8, 1/8) | $1.89122 \times 10^5$ | |
| b | *16c* | (0, 0, 0) | 0.05427 | +0.00270 |
| r | *16d* | (1/2, 1/2, 1/2) | 0.00260 | +0.00510 |
| c | *8b* | (3/8, 3/8, 3/8) | 0.00148 | +0.00315 |
| Pb | *8a* | (1/8, 1/8, 1/8) | $2.96523 \times 10^6$ | |
| b | *16c* | (0, 0, 0) | 0.03885 | +0.03082 |
| r | *16d* | (1/2, 1/2, 1/2) | 0.00166 | +0.00258 |
| c | *8b* | (3/8, 3/8, 3/8) | 0.00099 | +0.00162 |

[a] Wyckoff positions correspond to the $Fd\bar{3}m$ group. All values in atomic units.

**Table 8.** Topology of the Electron Density for the Non-Diamond Allotropes[a]

| CP | Wyckoff | position | $\rho(r_c)$ | $\nabla^2\rho(r_c)$ | x |
|---|---|---|---|---|---|
| C1 | *2b* | (0, 0, 1/4) | $1.28333 \times 10^2$ | | |
| C2 | *2c* | (1/3, 2/3, 1/4) | $1.28325 \times 10^2$ | | |
| $b_1$ | *2a* | (0, 0, 0) | 0.00588 | +0.01767 | |
| $b_2$ | *6h* | (x, 2x, 1/4) | 0.30199 | −0.88798 | 0.83316 |
| $r_1$ | *6g* | (1/2, 1/2, 0) | 0.00410 | +0.01400 | |
| $r_2$ | *2c* | (2/3, 1/3, 3/4) | 0.02271 | +0.13476 | |
| c | *4f* | (1/3, 2/3 x) | 0.00340 | +0.01317 | 0.47142 |
| Sn | *4a* | (0, 0, 0) | $1.89128 \times 10^5$ | | |
| $b_1$ | *4b* | (0, 0, 1/2) | 0.02838 | +0.01723 | |
| $b_2$ | *8c* | (0, 1/4, 1/8) | 0.03751 | +0.01222 | |
| $r_1$ | *8d* | (0, 1/4, 5/8) | 0.01303 | +0.01733 | |
| $r_2$ | *16f* | (x, 1/4, 1/8) | 0.00805 | +0.01397 | 0.29807 |
| c | *16g* | (x, x, 0) | 0.00803 | +0.01391 | 0.28456 |
| Pb | *4a* | (0, 0, 0) | $2.96493 \times 10^6$ | | |
| b | *24d* | (1/4, 1/4, 0) | 0.01788 | +0.02222 | |
| r | *32f* | (x, x, x) | 0.01287 | +0.01518 | 0.31837 |
| $c_1$ | *8c* | (1/4, 1/4, 1/4) | 0.01208 | +0.01361 | |
| $c_2$ | *4b* | (1/2, 1/2, 1/2) | 0.00674 | +0.00904 | |

[a] The Wyckoff positions correspond to the space groups $P6_3/mmc$ (graphite), $I4_1/amd$ (white Sn), and $Fm\bar{3}m$ (α-Pb).

the well-known trend of DFT GGA calculations. Ge and Sn in the diamond phase, and the graphite phase of C have a null band gap in our calculations, as it can be observed in Figure 2, but the Fermi level occurs in the limit of two bands, so the electronic density of states (DOS) is essentially zero at the Fermi level. White Sn and the fcc and diamond phases of Pb are completely different, with the Fermi level occurring in a energy region with a large DOS that confers a clear metallic behavior to these crystals.

The wave functions that we will analyze in the next sections correspond to the calculations performed at the experimental geometry. We have also examined the topological properties of the wave functions obtained from DFT LCAO calculations with the crystal code,[75,76] but given that the results are essentially equivalent, they will not be discussed again.

**6.2. Topology of the Electron Density.** Tables 7 and 8 describe the position and main properties of the critical points of the electron density for the diamond and nondiamond crystal structures of C−Pb. One of the most relevant observations is that all the diamond structures show the same topology, with a single type for each of *n*, *b*, *r*, and *c* critical points (NCP, BCP, RCP, and CCP, respectively), all of them occupying symmetry-defined positions within the unit cell. Once revealed this uniformity, the properties of the CPs clearly show important differences for each element. The electron density at the nuclear position shows a markedly correlation with the atomic number: $\rho_n = 0.11378Z^{3.7415}$, with a linear correlation coefficient of $corr(\rho, Z) = 99.4\%$, similar to the law cited by Bader[1] for nonrelativistic calculations. The properties at the BCP are particularly significant. The electron density at the BCP decreases as the cubic cell length increases: $\rho_b = 6.412656a^{-2.57024}$ (corr = −99.5%). The BCP Laplacian shows a well-defined trend in the C−Pb sequence, increasing from the negative −0.55144 e/bohr[5] of C, typical of a highly covalent bond, to the small but positive +0.03082 e/bohr[5] of Pb, closed-shell like and

similar to the values found in many metals. This negative/positive $\nabla^2\rho_b$ difference separates C, Si, and Ge on the covalent side, and Sn and Pb on the closed-shell group.

The non-diamond allotropes offer some fine aspects for contrast and comparison to the above crystals. Graphite, for instance, shows two different types of C−C BCPs: a strong bond that keeps together the graphene sheets, and a much weaker BCP gluing together the sheets. The first BCP has a larger electron density and a more negative Laplacian than the diamond structure, close, in fact, to the values shown by the C−C BCP in benzene. The β-Sn and α-Pb structures show a marked difference in topology with respect to their diamond crystals: the BCP is weaker (smaller $\rho_b$ and more positive $\nabla^2\rho_b$) and the electron density is globally flatter[77] ($f = \rho_c/\rho_b$ is 21.4% in β-Sn and 37.7% in α-Pb versus 2.7% and 2.5% in their respective diamond structures).

All together, we can see that the crystalline structure has a strong influence on the electron density topology, and that a clear group trend can be observed only after we examine the different elements on a common crystal phase.

**6.3. Topology of the *L(r)* Field.** One of the most remarkable aspects of the topology of the *L(r)* field is that the total number of critical points increases heavily with the atomic number of the atoms involved but the overall complexity, once the core CP's are discounted, does not follow this trend but rather it appears to depend on the nature of the bonding and, in general, it tends to diminish in going from the light to the heavy elements. This effect is evident in the topologies presented in Tables 9 and 10. The *L(r)* are grouped into core subshells when their distance to the closest atomic nucleus is quite close to the minima and maxima of the radial *L(r)* function. The core character of those CPs can be confirmed by the fact that the attraction basins of all core NCP's form a small sphere, as it will be discussed later.

The *L(r)* critical points (L-CPs) can be classified into core, valence and interstitial. A core subshell is formed by the breaking of one minimum or maximum of the atomic radial *L(r)* function, all CP's in the subshell keep an almost identical

**Table 9.** Topology of the $L(r)$ Field for the Diamond Structures[a]

| | | core: t | n | total: t | n | type | Wyckoff | $\mathbf{r}_{cp}$ | $\rho(\mathbf{r}_{cp})$ | $\nabla^2\rho(\mathbf{r}_{cp})$ | x coord. | z coord. |
|---|---|---|---|---|---|---|---|---|---|---|---|---|
| C | n | 1 | 8 | 3 | 48 | n | l | 8b | (3/8, 3/8, 3/8) | 0.013 24 | +0.075 95 | | |
| | b | 1 | 32 | 5 | 208 | n | val | 32e | (x, x, x) | 0.277 42 | −0.895 63 | 0.042 41 | |
| | r | 1 | 48 | 4 | 224 | b | bond | 16c | (0, 0, 0) | 0.240 05 | −0.551 44 | | |
| | c | 1 | 32 | 2 | 64 | b | l | 96g | (x, x, z) | 0.067 70 | +0.172 08 | 0.078 94 | 0.840 82 |
| | last | | K_ | | | b | l | 16d | (1/2, 1/2, 1/2) | 0.021 51 | +0.105 22 | | |
| | | | | | | b | val | 48f | (1/8, 1/8, x) | 0.213 00 | −0.197 58 | 0.269 23 | |
| | | | | | | r | val | 32e | (x, x, x) | 0.178 75 | +0.030 93 | 0.210 77 | |
| | | | | | | r | l | 96h | (x, \bbar\x\ebar\, 0) | 0.067 27 | +0.173 36 | 0.137 86 | |
| | | | | | | r | l | 48f | (1/8, 1/8, x) | 0.080 81 | +0.184 42 | 0.374 41 | |
| | | | | | | c | l | 32e | (x, x, x) | 0.078 47 | +0.206 77 | 0.254 24 | |
| Si | n | 2 | 40 | 4 | 80 | n | l | 8b | (3/8, 3/8, 3/8) | 0.003 24 | +0.008 97 | | |
| | b | 3 | 112 | 7 | 288 | n | val | 32e | (x, x, x) | 0.086 56 | −0.138 22 | 0.024 69 | |
| | r | 3 | 128 | 7 | 400 | b | bond | 16c | (0, 0, 0) | 0.083 69 | −0.123 44 | | |
| | c | 2 | 64 | 4 | 192 | b | l | 96g | (x, x, z) | 0.020 75 | +0.027 13 | 0.189 91 | 0.822 96 |
| | last | | L_ | | | b | l | 16d | (1/2, 1/2 1/2) | 0.055 89 | +0.013 54 | | |
| | | | | | | b | val | 48f | (1/8, 1/8, x) | 0.051 04 | −0.009 31 | 0.301 72 | |
| | | | | | | r | val | 32e | (x, x, x) | 0.036 73 | +0.017 55 | 0.231 47 | |
| | | | | | | r | l | 96h | (x, \bbar\x\ebar\, 0) | 0.021 51 | +0.027 49 | 0.364 84 | |
| | | | | | | r | l | 48f | (1/8, 1/8, x) | 0.022 02 | +0.027 93 | 0.386 10 | |
| | | | | | | r | l | 96g | (x, x, z) | 0.021 23 | +0.027 99 | 0.058 03 | 0.360 72 |
| | | | | | | c | l | 96g | (x, x, z) | 0.021 46 | +0.027 99 | 0.322 40 | 0.628 91 |
| | | | | | | c | l | 32e | (x, x, x) | 0.021 52 | +0.028 79 | 0.257 43 | |
| Ge | n | 3 | 72 | 5 | 96 | n | l | 8b | (3/8, 3/8, 3/8) | 0.002 57 | +0.006 52 | | |
| | b | 5 | 192 | 7 | 304 | n | bond | 16c | (0, 0, 0) | 0.075 02 | −0.035 56 | | |
| | r | 5 | 208 | 6 | 304 | b | l | 96g | (x, x, z) | 0.025 51 | +0.029 23 | 0.065 84 | 0.868 20 |
| | c | 3 | 96 | 3 | 96 | b | l | 16d | (1/2, 1/2, 1/2) | 0.004 36 | +0.010 21 | | |
| | last | | M_ | | | r | l | 96h | (x, \bbar\x\ebar\, 0) | 0.025 55 | +0.029 27 | 0.286 01 | |
| Sn | n | 4 | 104 | 6 | 128 | n | l | 8b | (3/8, 3/8, 3/8) | 0.001 48 | +0.003 15 | | |
| | b | 8 | 304 | 10 | 416 | n | bond | 16c | (0, 0, 0) | 0.054 27 | +0.002 70 | | |
| | r | 7 | 336 | 8 | 432 | b | l | 96g | (x, x, z) | 0.022 12 | +0.018 93 | 0.057 79 | 0.884 87 |
| | c | 4 | 144 | 4 | 144 | b | l | 16d | (1/2, 1/2, 1/2) | 0.025 98 | +0.005 01 | | |
| | last | | N_ | | | r | l | 96h | (x, \bbar\x\ebar\, 0) | 0.022 10 | +0.018 99 | 0.400 13 | |
| Pb | n | 5 | 136 | 6 | 144 | n | l | 8b | (3/8, 3/8, 3/8) | 0.000 99 | +0.001 62 | | |
| | b | 10 | 384 | 11 | 400 | b | l | 16d | (1/2, 1/2, 1/2) | 0.001 66 | +0.002 58 | | |
| | r | 8 | 416 | 9 | 432 | r | bond | 16c | (0, 0, 0) | 0.038 85 | +0.030 82 | | |
| | c | 5 | 176 | 5 | 176 | | | | | | | | |
| | last | | O_ | | | | | | | | | | |

[a] The left part of the table resumes the type ($t$) and number ($n$) of CPs included in the core and those in the whole crystal unit cell. *Last* is the identity of the last core subshell. The right part of the table is a detailed description of the valence CPs, classified into valence, bond (a kind of valence CP placed in the line between two atoms bonded by the $\rho(r)$ field), and interstitial (I, not recognizable as belonging to any single atom or pair of atoms). In the case of Pb, the algorithm fails to detect a RCP of multiplicity 96 in the L_ core shell, but the complete topology can be recovered from the invariance laws that rule shell and cell CPs.

distance to the originating nucleus, and the number of CP's fulfill the Euler relationship (eq 11). In addition, the attraction basins of the set of core NCP's form a small sphere around the nucleus, as it will be discussed later.

Valence L-CPs are originated from the outermost or perhaps the two outermost extrema of the atomic $L(\mathbf{r})$ radial function. The distance to the nucleus, however, is not so closely maintained as in the core case, and some CPs can be displaced toward the interatomic space, or even merged with the CP's from other nuclei, so the Euler relationship is not necessarily fulfilled by a valence subshell.

Interstitial L-CPs, finally, cannot be assigned to a single atom, but they lie well into the interatomic space. Interstitial NCP's, typically have a negative $L$ value, at difference from core and valence NCP's. In other words, interstitial NCP's do not show an increased concentration of electron density relative to their differential neighborhood. This counterintuitive property turns to be one of the most prominent features of interstitial regions.

6.3.1. *Graphs for the L(r) Topology.* The complexity of the $L(r)$ topology is difficult to examine without an appropriate map. Aray et al.[78−82] and Popelier et al.[6,11,31,33] have taken great advantage of special chemical graphs for that purpose. Drawing a significant $L$ graph is not trivial nor automatic, but it involves some creative decisions about what information is relevant and what should be left out to avoid cluttering.

Figures 3 and 4 shows our interpretation of the relevant $L(r)$ topology for the diamond and non-diamond structures. Some of the most relevant features correspond to the organization of the valence L-BCPs and the bond paths that connect them to the NCPs. Many of those $L$-bond paths are quite curved lines. In particular, bond paths that connect NCPs in the same subshell and thus are equidistant to the generating nucleus are almost circular arcs. This sharply contrast with the $\rho$-bond paths that are typically straight lines and do only curve away from the internuclear axis in such cases as the occurrence of steric stress or electron deficient bonding.[1]

**Table 10.** Topology of the $L(\mathbf{r})$ Field for the Non-diamond Allotropes[a]

|  | core: | t, n | total: | t, n | type | /Wyckoff |  | $r_{cp}$ | $\rho(r_{cp})$ | $\nabla^2\rho(r_{cp})$ | x coord. | z coord. |
|---|---|---|---|---|---|---|---|---|---|---|---|---|
| graphite | n | 2 4 | 5 | 20 | n | l | 4f | (1/3, 2/3, z) | 0.003 48 | +0.012 72 | 0.482 23 | |
| | b | 2 12 | 10 | 70 | n | val | 6h | (x, 2x, 1/4) | 0.323 37 | −1.132 02 | 0.881 25 | |
| | r | 2 12 | 10 | 70 | n | val | 6h | (x, 2x, 1/4) | 0.322 96 | −1.126 87 | 0.785 52 | |
| | c | 2 8 | 4 | 20 | b | l | 6h | (x, 2x, 1/4) | 0.301 99 | −0.887 98 | 0.833 29 | |
| | last | K_ | | | b | l | 4f | (1/3, 2/3, z) | 0.068 83 | +0.113 31 | 0.628 53 | |
| | | | | | b | l | 12k | (x, 2x, z) | 0.071 78 | +0.117 92 | 0.175 76 | 0.860 34 |
| | | | | | b | val | 12k | (x, 2x, z) | 0.179 63 | −0.096 52 | 0.393 24 | 0.680 88 |
| | | | | | b | l | 2c | (1/3, 2/3, 1/4) | 0.022 71 | +0.134 76 | | |
| | | | | | b | val | 12k | (x, 2x, z) | 0.180 45 | −0.091 11 | 0.064 66 | 0.182 65 |
| | | | | | b | l | 4e | (0, 0, z) | 0.068 60 | +0.114 73 | 0.128 69 | |
| | | | | | b | l | 6g | (1/2, 0, 0) | 0.004 10 | +0.014 00 | | |
| | | | | | r | val | 6h | (x, 2x, 1/4) | 0.210 27 | −0.015 96 | 0.544 96 | |
| | | | | | r | l | 12j | (x, y, 1/4) | 0.079 57 | +0.235 37 | 0.560 98 | 0.667 06 |
| | | | | | r | val | 6h | (x, 2x, 1/4) | 0.210 88 | −0.020 57 | 0.121 58 | |
| | | | | | r | val | 4f | (1/3, 2/3, z) | 0.166 11 | −0.084 69 | 0.670 25 | |
| | | | | | r | val | 4e | (0, 0, z) | 0.164 37 | −0.076 57 | 0.170 07 | |
| | | | | | r | l | 12k | (x, 2x, z) | 0.074 52 | +0.118 05 | 0.206 44 | 0.640 14 |
| | | | | | r | l | 12k | (x, 2x, z) | 0.074 67 | +0.118 47 | 0.118 31 | 0.860 22 |
| | | | | | r | l | 2a | (0, 0, 0) | 0.005 88 | +0.017 67 | | |
| | | | | | c | l | 6h | (x, 2x, 1/4) | 0.092 22 | +0.252 29 | 0.475 98 | |
| | | | | | c | l | 6h | (x, 2x, 1/4) | 0.092 10 | +0.251 88 | 0.190 86 | |
| β-Sn | n | 4 52 | 7 | 80 | n | l | 16g | (x, x, 0) | 0.008 03 | +0.013 91 | 0.285 99 | |
| | b | 11 144 | 15 | 208 | n | bond | 8c | (0, 1/4, 1/8) | 0.037 51 | +0.012 23 | | |
| | r | 10 144 | 13 | 184 | n | bond | 4b | (0, 0, 1/2) | 0.028 38 | +0.017 23 | | |
| | c | 4 56 | 4 | 56 | b | l | 16h | (0, y, z) | 0.014 33 | +0.017 03 | 0.199 36 | 0.518 18 |
| | last | N_ | | | b | l | 16h | (0, y, z) | 0.021 95 | +0.018 52 | 0.098 24 | 0.497 51 |
| | | | | | b | l | 16f | (x, 1/4, 1/8) | 0.008 05 | +0.013 97 | 0.296 43 | |
| | | | | | b | l | 16h | (0, y, z) | 0.022 07 | +0.018 92 | 0.212 11 | 0.362 60 |
| | | | | | r | l | 8d | (0, 1/4, 5/8) | 0.013 03 | +0.017 34 | | |
| | | | | | r | l | 16f | (x, 1/4, 1/8) | 0.019 99 | +0.020 12 | 0.138 57 | |
| | | | | | r | l | 16g | (x, x, 0) | 0.020 38 | +0.018 88 | 0.422 20 | |
| α-Pb | n | 5 132 | 7 | 144 | n | l | 4b | (1/2, 1/2, 1/2) | 0.006 74 | +0.009 04 | | |
| | b | 9 336 | 10 | 368 | n | l | 8c | (1/4, 1/4, 1/4) | 0.012 08 | +0.013 61 | | |
| | r | 9 336 | 10 | 360 | b | l | 32f | (x, x, x) | 0.012 72 | +0.015 29 | 0.336 65 | |
| | c | 5 136 | 5 | 136 | r | l | 24d | (0, 1/4, 1/4) | 0.017 88 | +0.022 22 | 0.833 29 | |
| | last | O_ | | | | | | | | | | |

[a] See description in Table 9.

Another striking difference between the *L* and $\rho$ graphs is that while the five elements, C to Pb, shows identical $\rho$ graph in the diamond phase, their *L* graph can be grouped into three quite different models. C and Si form the first model, that closely resembles a prototypical Lewis image for covalent bonding: each atom is surrounded by a curved tetrahedron frame with NCP's at the vertices. Each NCP is then connected through a *L*-bond path to the NCP of a nearest neighbor (NN) atom. As a consequence, the middle point between two NN atoms (the 16c Wyckoff position in Table 7 and Table 9) is simultaneously a $\rho$-BCP and a L-BCP. Furthermore, this double BCP occurs in a region of significant local charge accumulation, thus completing the characterization of the C and Si *L* graph as a prototype of covalently bonded system.

This Wyckoff *16c* position has the key to characterize the three types of *L* graphs in the diamond structure. The second type is shown by Ge and Sn, where the *16c* point continues to be a $\rho$-BCP but it is now a L-NCP, connected through *L* bond paths to six other equivalent *16c* positions. At the same time, the outermost valence shell of each atom is now made of a tetrahedron of CCPs rather than NCPs.

Pb diamond phase shows the third kind of *L* graph. The Pb core is quite large, and the only noncore NCPs have moved into the interstitial region. The *16c* position is now a ring CP and corresponds to a corner in which four interstitial NCP basins intersect. The valence electron density has been maximally delocalized and transferred to the interstitial region.

The nondiamond phases behave like their diamond equivalents. C shows again in the graphite phase a covalent pattern, with two bonded NCPs along the internuclear axis, the $\rho$-BCP and the L-BCP occurring at the same position, within a region of increased electron density concentration. Of course, rather than a tetrahedral pattern, NCPs form now a flat triangle surrounding each C nucleus. In Mulliken terms, the $sp^3$ arrangement has been converted into a $sp^2$ one. White Sn and fcc Pb also show the same pattern as their corresponding diamond phases.

As described in section 4, the shape of the valence electron density is affected by the relativistic treatment of the crystal. To measure the sensitivity of *L* graphs to this effect, we have recalculated Sn and Pb in both diamond and experimental phases without the scalar relativistic correction. The *L* topology of Sn is unaffected in the diamond phase, while the changes in the β-Sn phase are minor: a L-BCP bonding two interstitial maxima and a L-RCP are displaced to a lower symmetry position, without any significant consequence on the preceding discussion. The effect is more pronounced on both phases of Pb. In the fcc phase, a number of new CP

Electron Density Laplacian

*J. Chem. Theory Comput., Vol. 6, No. 12, 2010* **3773**
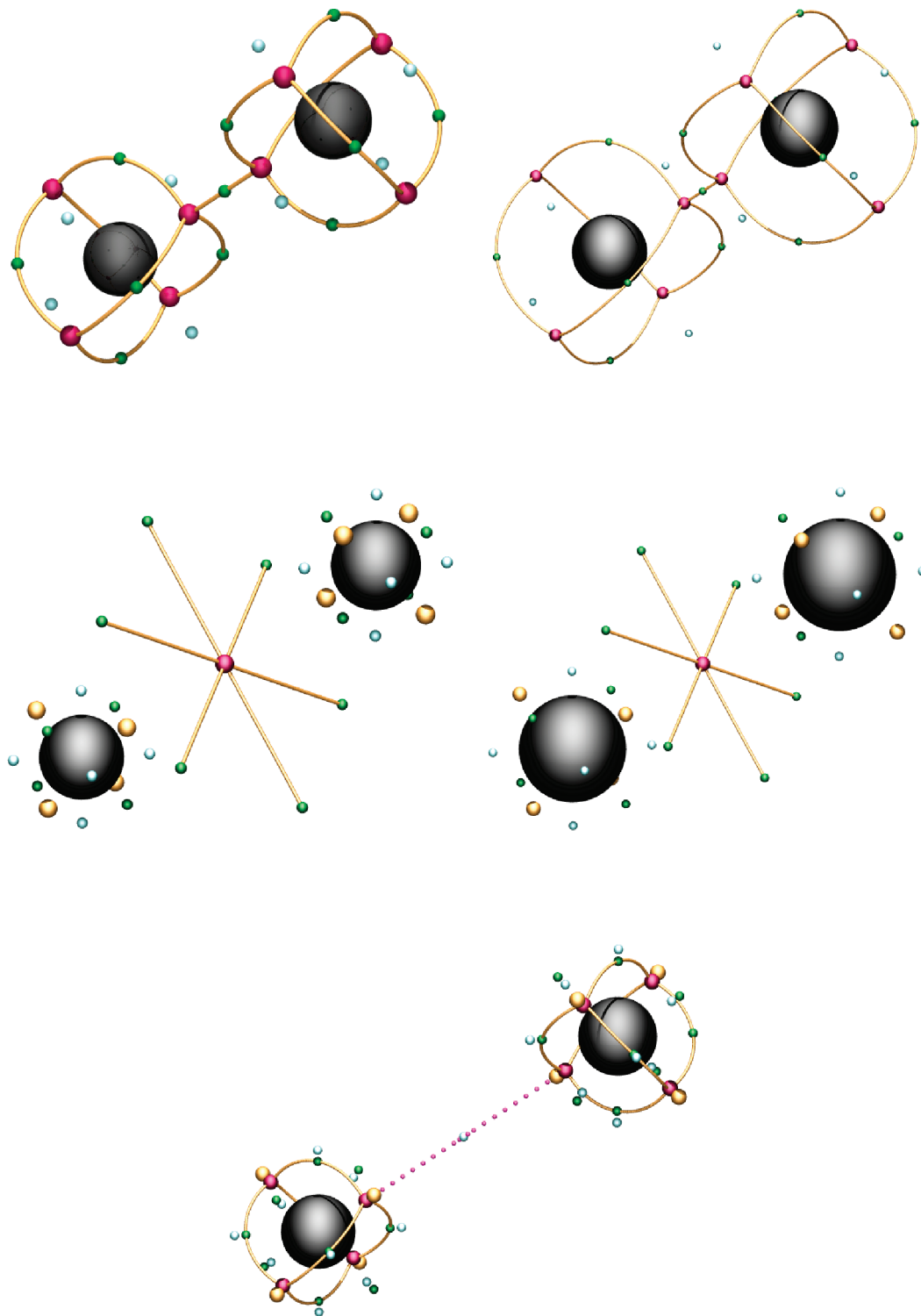


**Figure 3.** *L* graphs for the diamond structures (top, C and Si; middle, Ge and Sn; bottom, Pb). The very large black spheres contain the nuclei and most of the core structure. Far smaller, L-CPs can be discriminated by the size and color of the spheres that represent them: NCPs are large and dark (red), BCPs smaller and dark (green), RCPs small and light (light blue), and CCPs large and light (yellow). *L*-bond paths are sometimes represented by thin golden lines. The Pb-diamond graph shows the *L* ring path, created by the RCP lying in the middle of two nearest neighbors Pb atoms, as a discontinuous line of very thin spheres (pink).

appear, the most important of them being a new interstitial maximum at the (0, 1/4, 1/4) (24d) position. In the diamond phase, the *16c* maximum reappears, resulting in Pb having a graph equivalent to Ge and Sn. The greater effects of the relativistic corrrection in heavier elements couples in this case with the well-known lability of the topology of ρ (and

hence *L*) in metals:[83] the flatness of the interstitial part induces that even small density changes rearrange the valence topology completely.

Far less important is the effect of changing the exchange-correlation functional. The topologies of all the crystals examined are unaffected when calculated at the LDA level.
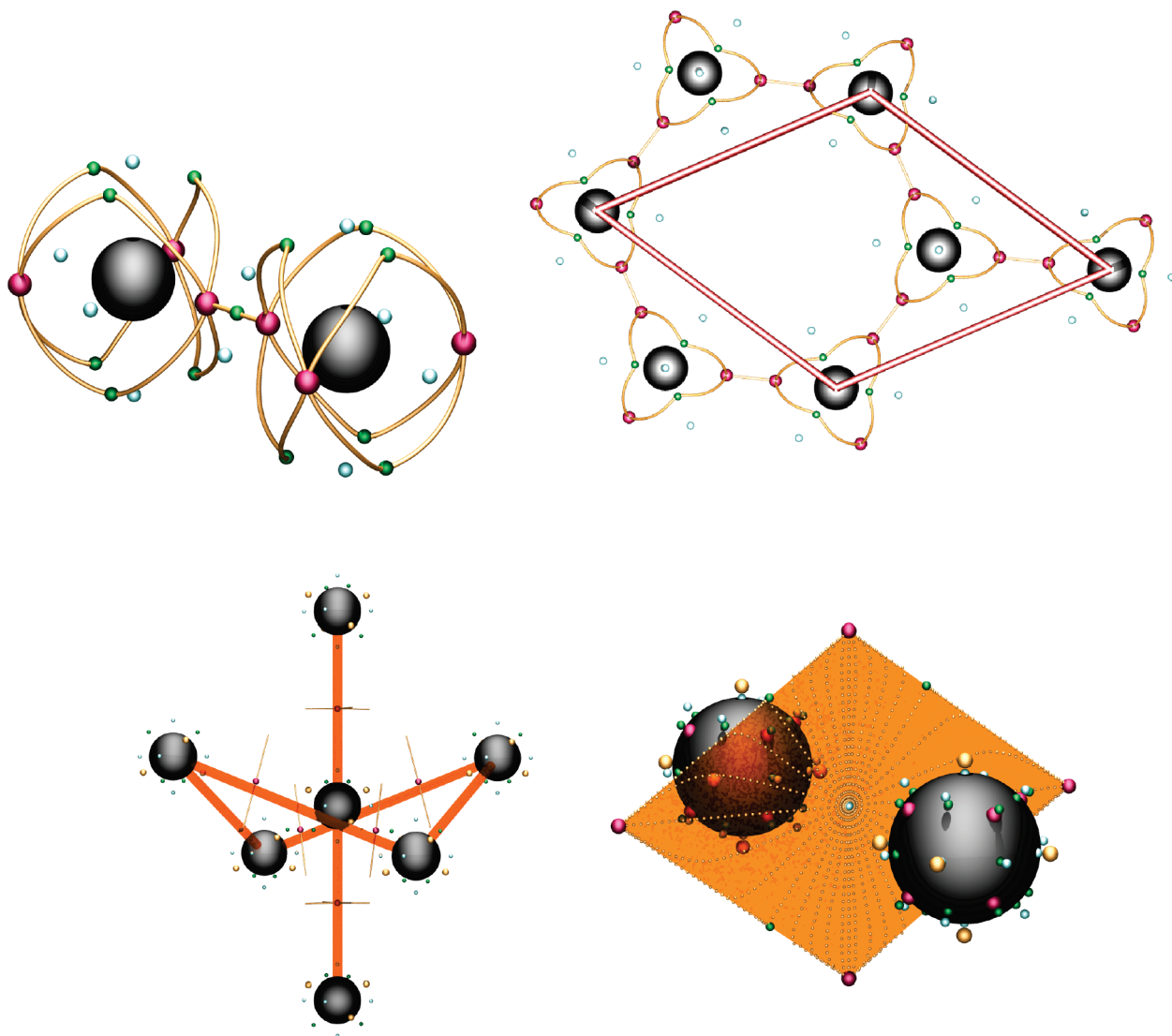
**Figure 4.** *L* graphs for the non-diamond structures (upper row, graphite; lower row, white Sn and fcc Pb). The zenithal view of graphite shows the crystal unit cell using thick cylinders. The Pb-fcc graph shows the equivalent RCP surface and the graph lines that form this surface.

*6.3.2. Local Properties of the L-NCP Basins.* The number, arrangement, and properties of NCPs is the central issue of the $L(r)$ topology. The $L$ graphs analyzed previously fail to communicate the shape, size, and relative importance of the NCP basins. All L-NCPs in the diamond phase are placed along the cube diagonal, that is, along the $(x, x, x)$ crystal direction. We have taken advantage of this coincidence to produce the illustration in Figure 5. The plots show clearly the difference between the three types of $L$ graphs described in the previous subsection (6.3.1). The twin L-NCPs between two NN atoms observed on C and Si, get converted into a single NCP at the NN midpoint on Ge and Sn, and finally the internuclear axis is simply the common edge of four interstitial NCPs on Pb.

Figure 5 is also a qualitative demonstration of the growing importance of the interstitial NCP as the atomic number increases. The core region increases too and, more interesting, the core subshells form concentric spheres that surround the atomic nucleus. That a given shell keeps the spherical shape typical of a free atom can be seen as the ultimate evidence that it belongs in the core. Contrarily, a significant deforma-

tion from sphericity is a direct proof of the participation of the corresponding electrons in the valence chemical bonding.

Going beyond the qualitative requires integrating properties within the $L$ basins. In this regard it must be clear that there is a fundamental difference between the space partition induced by $\rho(r)$ and the partition due to $L(r)$. All kind of quantum mechanical observables can be integrated within the basins determined by the zero flux of $\rho(r)$ condition (eq 3). This is not true for the basins determined by the topology of $L(r)$ and, for instance, it is not correct to determine the contribution of a L-NCP basin to the kinetic energy. There is no problem, however, with the integration of strictly local properties like the volume, charge, electrostatic field, or multipolar moments.

Table 11 presents the volume and electronic populations of the L-NCP basins. We have classified the basins into five different groups according to its properties: nucleus, core, valence, bond, and interstitial. The nucleus can include some L-NCP so internal that we have preferred not to distinguish them from the atomic position. The "valence" L-NCPs correspond to the twin maxima situated along a NN inter-
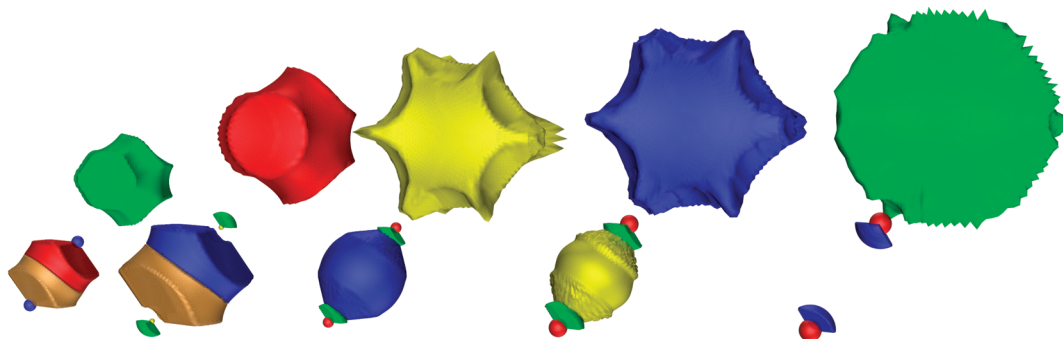
**Figure 5.** From left to right: L-NCP basins of C, Si, Ge, Sn, and Pb in the diamond phase. All plots are made in the same scale, and use the same viewpoint, so the apparent relative size corresponds to the actual size of the basins. The two small spheres appearing in all the plots correspond to the atomic core regions; between them we can find the single or double "bond" L-NCP, absent in the case of Pb; the uppermost basin is, in all cases, the interstitial L-NCP.

**Table 11.** Volume ($V_\Omega$, bohr$^3$) and Electronic Population ($Q_\Omega$, e) of the L-NCP Basins$^a$

| | | | | | | | | | | | |
|---|---|---|---|---|---|---|---|---|---|---|---|
| | | | | | diamond phase | | | | | | |
| type | Wyckoff | C: $Q_\Omega$ | $V_\Omega$ | Si: $Q_\Omega$ | $V_\Omega$ | Ge: $Q_\Omega$ | $V_\Omega$ | Sn: $Q_\Omega$ | $V_\Omega$ | Pb: $Q_\Omega$ | $V_\Omega$ |
| nuc. | 8a | 0.988 | 0.051 | 1.049 | 0.004 | 8.060 | 0.043 | 24.078 | 0.245 | 51.264 | 0.508 |
| core | 32e | | | 1.561 | 0.224 | 3.428 | 0.423 | 4.017 | 1.319 | 4.658 | 1.343 |
| val. | 32e | 1.078 | 5.144 | 1.511 | 18.628 | | | | | | |
| bond | 16c | | | | | 3.163 | 22.210 | 2.331 | 22.789 | | |
| I | 8b | 0.707 | 17.630 | 0.658 | 59.722 | 3.931 | 106.627 | 5.260 | 179.806 | 11.959 | 290.608 |
| total | | 48.053 | 306.050 | 111.946 | 1081.074 | 256.226 | 1222.259 | 400.534 | 1847.233 | 654.836 | 2371.890 |
| cell | | 48.000 | 306.217 | 112.000 | 1080.847 | 256.000 | 1221.900 | 400.000 | 1845.744 | 656.000 | 2373.614 |
| error | | 0.053 | −0.167 | −0.054 | 0.227 | 0.226 | 0.359 | 0.534 | 1.488 | −1.164 | −1.724 |
| % | | 0.111 | −0.055 | −0.048 | 0.021 | 0.088 | 0.029 | 0.133 | 0.081 | −0.177 | −0.073 |

| | | | | | | | | | |
|---|---|---|---|---|---|---|---|---|---|
| | | | | | non-diamond phase | | | | |
| graphite | | $Q_\Omega$ | $V_\Omega$ | white Sn | | $Q_\Omega$ | $V_\Omega$ | fcc Pb | | $Q_\Omega$ | $V_\Omega$ |
| C | 2b | 0.988 | 0.051 | Sn | 4a | 40.113 | 5.513 | Pb | 4a | 51.281 | 0.509 |
| C | 2c | 0.988 | 0.051 | bond | 4b | 0.966 | 11.184 | core | 32f | 2.342 | 0.688 |
| val. | 6h | 1.348 | 5.891 | bond | 8c | 1.816 | 20.004 | | 8c | 2.401 | 36.549 |
| val. | 6h | 1.348 | 5.891 | I | 16g | 1.344 | 31.188 | I | 4b | 7.174 | 125.556 |
| I | 4f | 0.960 | 41.259 | | | | | | | | |
| total | | 23.969 | 235.931 | total | | 200.350 | 725.832 | total | | 327.969 | 818.660 |
| cell | | 24.000 | 236.048 | cell | | 200.000 | 725.647 | cell | | 328.000 | 818.736 |
| error | | −0.031 | 0.116 | error | | 0.350 | 0.186 | error | | −0.031 | −0.076 |
| % | | −0.130 | 0.049 | % | | 0.175 | 0.026 | % | | −0.009 | −0.009 |

$^a$ Notice that the calculation of the total properties has been made using partial data with more digits than those shown in the table. The properties reported correspond to single basins of each type and must be multiplied by the Wyckoff multiplicity to determine the contribution to the cell property.

nuclear axis. They are characterized by a positive value of $L(r)$ and belong, accordingly, to the region called VSCC (Valence Shell Charge Concentration) by Bader.[1] The single "bond" L-NCP, situated midway between NN atoms, can have a positive (Ge) or negative (Sn) $L(r)$ value. The last type of L-NCPs, finally, are disconnected from the $L$ graphs of nuclei, belong to the interstitial region and have, in all cases, a negative $L(r)$ value.

This classification of L-NCP basins is quite relevant for the analysis of the local properties. The nuclear and core $L$-NCP's occupy a very small volume but contain a significant number of the electrons. Valence (C and Si) and bond (Ge and Sn) NCP's occupy a part of the cell and contain some 2−3 electrons for each NN pair of atoms. The interstitial NCP's, finally, represent most of the cell volume and contain an electron population that grows from 0.7 $e$ in C and Si to a shocking 12 $e$ per NCP in Pb.

The important electron population of interstitial regions is not particular to crystals, but it was already observed by Malcolm and Popelier[34] in molecules like $NH_3$ and $H_2O$. This fact, which Malcolm and Popelier elude to interpret, is one of the problematic features if we try to explain the $L$ populations in terms of a simple Lewis model.

In a classical Lewis description, each C in the diamond structure uses four electrons to form the same number of covalent bonds to its NN, remaining two nonbonding electrons on each C core. Our topological analysis of $L(r)$ shows a small excess of 0.08 $e$ involved per C on each covalent bond, but a donation of 0.71 $e$ per C toward the interstitial space.

The comparison with the Lewis model is even worse in Si. Now each Si atom uses 1.5 $e$ to form each of its four covalent Si−Si bonds. The donation to the interstitial space is quite similar to the diamond case, however, 0.66 $e$ per Si

atom. Ge and Sn also accumulate an extra number of electrons on the NN internuclear space: 3.16 $e$ (Ge) and 2.33 $e$ (Sn) rather than the two electrons expected for a classical Lewis single covalent bond. The donation to the interstitial space is significantly increased: 3.93 $e$ in Ge and 5.26 $e$ in Sn. Finally, Pb lacks the features that could be described as covalent bonds. Contrarily, all the electrons removed from the nuclear and core regions now belong to the interstitial zone: a record 11.96 $e$ per Pb atom.

It is tempting to explain this behavior of group IV elements as successive steps in the conversion from covalent to metallic bonding. The small population of the interstitial zones, similar to the values previously reported for some covalent molecules,[34,34] could be regarded as the minimal background. Some more cases, and more diverse crystals and molecules, should be analyzed before this conjecture can be accepted, however.

The changes induced by the scalar relativistic treatment of valence electrons are apparent by comparing the Sn and Pb results to its nonrelativistic counterparts. It was mentioned in section 4 that the $L$-graphs are not compatible, so the comparison is not direct. However, several observations can be made about these differences: (1) The shell radii are contracted; the nucleus plus the inner shells loses approximately 0.1 electrons in Sn, and almost 1 electron in Pb. (2) The bond basins shrink and lose electrons, the charge smearing out to the interstitial basins.

The effect of changing the exchange-correlation potential is, again, not as significant. The cores are almost unaffected, with a difference in core population that peaks at 0.03 electrons in Pb, with an analogous behavior of the outer core basins. Regarding the valence and interstitial basins, LDA assigns less charge to the valence and bond basins, with slightly larger and more populated interstitial basins than GGA. The differences between both functionals increase on advancing to the heavier elements of the group. Exchange-correlation and relativistic effects are certainly interesting and, hopefully, will be addressed in a future work, once the utility of the present methodology is established.

The comparison between the two different phases of C, Sn and Pb opens an important window for analyzing the transferability of L-NCP basin properties among distinct structures and compounds. Diamond and graphite are very dissimilar in their bonding pattern and cell volume per atom (38.3 vs 59.0 bohr$^3$, respectively), but the nuclear L-NCP is almost identical in both crystals ($Q = 0.9875$ vs 0.9882 $e$, $V = 0.0512$ vs 0.0512 bohr$^3$), the single bond L-NCP has a similar number of electrons per C atom (4.31 vs 4.04 $e$) even though this region occupies a larger volume in the more dense diamond phase than in the less dense graphite (20.6 vs 17.7 bohr$^3$) and, finally, the larger differences occur between the corresponding interstitial L-NCP ($Q = 0.71$ vs 0.96 $e$, $V = 17.6$ vs 41.3 bohr$^3$).

This scheme is repeated on Sn and Pb. The transferability of properties between different structures is almost exact for the nuclear and core L-NCP basins. Bond and valence L-NCP show significant regularities, although we need a larger set of compounds to extract the organizing principles. The interstitial L-NCP basins, the most unexpected topological

feature of the Laplacian, is also the most variable element, and much study is required before its role can be clarified.

*6.3.3. Local Compressibilities of the L-NCP Basins.* The tetrahedral arrangement of covalently bonded C atoms has been usually called to explain the extreme hardness of diamond. The same arrangement, however, does not explain the large hardness differences between the isostructural group IV elements. We can gain some insight into the phenomenon by determining the contribution of the several L-NCP basins to the elastic properties. We will follow the method proposed by Martn Pendás et al. on the analysis of $\rho(\mathbf{r})$[84,85] and recently applied by Recio et al. to the ELF function.[86]

The static compressibility ($\kappa$) and bulk modulus ($B$) of a crystal are defined as

$$\kappa = \frac{1}{B} = -\frac{1}{V}\left(\frac{\partial V}{\partial p}\right) \tag{20}$$

Using in these definitions the partition of the cell volume into L-NCP basin contributions, $V = \Sigma_\Omega V_\Omega$, we can write[84]

$$\kappa = \sum_\Omega f_\Omega \kappa_\Omega \text{ and } \frac{1}{B} = \sum_\Omega f_\Omega \frac{1}{B_\Omega} \tag{21}$$

where $f_\Omega = V_\Omega/V$ is the fraction of the cell volume occupied by the $\Omega$ basin, and

$$\kappa_\Omega = \frac{1}{B_\Omega} = -\frac{1}{V_\Omega}\left(\frac{\partial V_\Omega}{\partial p}\right) \tag{22}$$

The local compressibility of a basin is thus defined in the same way that the compressibility of the whole cell, and the global value of the crystal is the result of averaging the local compressibilities in such a way that the contribution of a basin is proportional to the volume fraction of the basin in the crystal cell.

To determine the local compressibilities of the group IV crystals we have followed the static model, in which the vibrational entropy is neglected by assuming a temperature of zero Kelvin, and the zero point vibrational energy is also neglected. Under these conditions the pressure is given by

$$p = -\left(\frac{\partial A}{\partial V}\right)_T \approx -\left(\frac{\partial E}{\partial V}\right) \tag{23}$$

where $V$ and $E$ are the cell volume and energy, result from the quantum mechanical calculation, and $A = E + A_{vib}(T, V) \approx E$ would have been the Helmholz free energy.

The actual sequence of calculations goes as follows. First, some $11-15$ points of the $E(V)$ curve are determined, with the volume bracketing a range of $\pm 10\%$ around the experimental geometry. Once verified that this range effectively contains the equilibrium volume, the pressure is obtained from eq 23, using a polynomial or a Birch−Murnaghan function to fit the calculated $E(V)$ points. Simultaneously, a topological analysis is performed on each wave function and the volumes of the L-NCP basins are determined. The $V(p)$ and $V_\Omega(p)$ data are used to evaluate the crystal and the local compressibilities, with a polynomial fitting to the data being again instrumental in obtaining the derivatives. The results from this analysis are presented in Table 12.

Electron Density Laplacian

*J. Chem. Theory Comput., Vol. 6, No. 12, 2010* **3777**

***Table 12.*** Volume Fraction ($f_\Omega$, %) and Local Compressibility ($\kappa_\Omega$, TPa$^{-1}$) of the L-NCP Basins[a]

| | | diamond phase: | | | | | | | | | |
|---|---|---|---|---|---|---|---|---|---|---|---|
| type | Wyckoff | C: $f_\Omega$ | $\kappa_\Omega$ | Si: $f_\Omega$ | $\kappa_\Omega$ | Ge: $f_\Omega$ | $\kappa_\Omega$ | Sn: $f_\Omega$ | $\kappa_\Omega$ | Pb: $f_\Omega$ | $\kappa_\Omega$ |
| nuc. | *8a* | 0.133 | 0.008 | 0.003 | 0.004 | 0.026 | 0.021 | 0.098 | 0.004 | 0.172 | 0.019 |
| core | *32e* | | | 0.648 | 0.018 | 1.043 | 0.005 | 2.116 | 0.083 | 1.811 | 0.210 |
| val. | *32e* | 54.126 | 1.255 | 55.447 | 5.123 | | | | | | |
| bond | *16c* | | | | | 28.356 | 8.074 | 18.739 | 15.157 | | |
| I | *8b* | 45.834 | 3.876 | 44.180 | 20.563 | 70.812 | 22.665 | 79.211 | 31.504 | 98.356 | 42.614 |
| $\kappa_t$ | | | 2.456 | | 11.926 | | 18.339 | | 27.797 | | 41.917 |
| $\kappa_0$ | | | 2.330 | | 11.977 | | 19.275 | | 29.406 | | 39.531 |
| $B_t$ | | | 407.210 | | 83.853 | | 54.528 | | 35.976 | | 23.857 |
| $B_0$ | | | 429.240 | | 83.492 | | 51.882 | | 34.006 | | 25.297 |

| | | non-diamond phase | | | | | | | |
|---|---|---|---|---|---|---|---|---|---|
| type | Wyckoff | C: $f_\Omega$ | $\kappa_\Omega$ | Wyckoff | Sn: $f_\Omega$ | $\kappa_\Omega$ | Wyckoff | Pb: $f_\Omega$ | $\kappa_\Omega$ |
| nuc. | *2b* | 0.043 | 0.013 | *4a* | 0.127 | 0.002 | *4a* | 0.234 | 0.012 |
| nuc. | *2c* | 0.043 | 0.013 | | | | | | |
| core | | | | *4b* | 5.761 | 0.853 | *32f* | 2.535 | 0.149 |
| core | | | | *16h* | 2.741 | 0.183 | | | |
| val. | *6h* | 14.861 | 1.926 | *8c* | 20.806 | 9.149 | | | |
| val. | *6h* | 14.874 | 1.936 | | | | | | |
| I | *4f* | 70.146 | 4.461 | *16g* | 70.384 | 28.597 | *8c* | 36.127 | 28.784 |
| I | | | | | | | *4b* | 61.246 | 24.185 |
| $\kappa_t$ | | | 3.704 | | | 22.085 | | | 25.215 |
| $\kappa_0$ | | | 3.662 | | | 20.660 | | | 28.226 |
| $B_t$ | | | 270.000 | | | 45.280 | | | 39.659 |
| $B_0$ | | | 273.070 | | | 48.403 | | | 35.429 |

[a] The bulk moduli are given in GPa. The topological $\kappa_t$ and $B_t$ values are obtained using eq 21. The values of $\kappa_0$ and $B_0$ are obtained from the total cell energy and volume according to eq 20. The difference between $B_t$ and $B_0$ is consequence of small errors in the determination of the basin volumes.

The results in Table 12 provide an excellent confirmation of the classification of the L-NCPs. Nuclear and core NCPs fill a small fraction of the cell volume and, more significantly, have a very small compressibility, less than 1% of the value of $\kappa$ for the whole crystal. In sharp contrast, the values of $\kappa_\Omega$ for the valence, bond, and interstitial L-NCPs are of the same order of magnitude than $\kappa$, smaller in the case of valence and bond regions and larger in the case of interstitial ones.

Restricting our analysis to the diamond phase, the extreme hardness of C is the consequence of the small compresibility of all the L-NCP regions. C and Si show a similar contribution balance, $f_{val} = 54-55\%$ and $f_I = 46-44\%$, but the $\kappa_\Omega$ values are several times larger in Si than in C. Ge and Sn show both the progressive increase in the coefficient of the interstitial zone and the increase of the $\kappa_\Omega$ values for all the zones. Finally, the soft metal character of Pb is almost exclusively because of the large and quite compressible interstitial regions.

Graphite shows clearly the importance of the crystalline structure. Compared with the diamond phase, graphite presents an interstitial zone larger and more compressible. The atomic number, however has a similar or larger influence, so the search for truly hard compounds can be restricted to the lightest elements. A topological partition of the shear modulus could be of interest as it would show the graphene sheets hard compared to the larger compressibility perpendicular to the sheets. We are working toward achieving a practical way of partitioning the elastic constants of arbitrary crystals.

$\beta$-Sn and $\alpha$-Pb, being significantly more dense than their diamond allotropes, show also a larger value for the bulk modulus, discarding the exclusive influence of the tetrahedral coordination on the hardness of group IV elements. To be fair in this conclusion, we should remember that $\beta$-Sn and $\alpha$-Pb show a metallic rather than covalent behavior and the hardness of single crystals is mostly controlled by the shear and not by the bulk modulus.

Diamond and nondiamond phases agree, anyway, on the fundamental importance of the interstitial regions in determining the bulk modulus and compressibility of crystals.

## 7. Conclusions and Perspectives for Future Work

The topology of $L(r)$ is far more complex than the topology of $\rho(r)$. First, $L(r)$ retains the shell structure inherited from the isolated atoms. Second, the range of $L(r)$ goes from $-\infty$ to $+\infty$, giving rise to maxima, for instance, with $L < 0$ and others with $L > 0$, both having a different chemical interpretation. Third, $L(r)$ has more critical points than $\rho(r)$, and their number increases heavily with the atomic number of the element. Fourth, $L$ basins tend to be more irregular, and the source or sink point of the basin can be separated from the geometrical center, thus leading to a more difficult integration of the basin properties.

Taking advantage of the shell structure is important in designing and adapting efficient algorithms, like the radial navigation method presented in section 5. It is also particularly important for simplifying the analysis and presentation of the $L(r)$ topology by removing unimportant core features in a controlled way. Basin plots (Figure 3) and $L$ graphs (Figure 5) have been found to be fundamental instruments

**3778** *J. Chem. Theory Comput., Vol. 6, No. 12, 2010*

Otero-dela-Roza and Luaña

to understand the organization and qualitative importance of the topological features of $L(r)$.

The electron density Laplacian provides a perspective that complements and is not directly available from the electron density. This is clearly observed in the group IV diamond phases. Whereas all, C to Pb, elements show identical topology for $\rho(r)$, the analysis of $L(r)$ evidence deep differences between the three groups formed by C and Si (the covalent group), Ge and Sn (the semilocal group), and Pb (the most delocalized one). This difference between the elements is transferred to other phases, showing the dominant influence of the nature of the element on $L(r)$, rather than the effect of the crystal geometry, more akin to influence the $\rho(r)$ topology.

Our topological methodology is mature enough for application to general crystals. Further work should now be directed to examine the $\rho(r)$ and $L(r)$ topologies in a diverse set of crystal types with an objective pointed toward solving some of the puzzles observed on group IV crystals. In particular, the role of interstitial regions and the contrast between the Lewis model and the real electron population on each basin.

## References

(1) Bader, R. F. W. *Atoms in Molecules. A Quantum Theory*; Oxford University Press: Oxford, U.K., 1990.

(2) Popelier, P. L. A. *Atoms in Molecules: An Introduction*; Prentice Hall: London, 2000; p 188.

(3) Boyd, R.; Matta, C. *The Quantum Theory of Atoms in Molecules: From Solid State to DNA and Drug Design*; Wiley-VCH: Weinheim, Germany, 2007.

(4) Bader, R. F. W. *Chem. Rev.* **1991**, *91*, 893–928.

(5) Bader, R. F. W. *Theor. Chem. Acc.* **2001**, *105*, 276–283.

(6) Popelier, P. L. A. *Coord. Chem. Rev.* **2000**, *197*, 169–189.

(7) Cortés-Guzmán, F.; Bader, R. F. W. *Coord. Chem. Rev.* **2005**, *249*, 633–662.

(8) Merino, G.; Vela, A.; Heine, T. *Chem. Rev.* **2005**, *105*, 3812–3841.

(9) Coppens, P. *X-Ray Charge Densities and Chemical Bonding*; IUCr and Oxford U. P.: New York, 1997.

(10) Popelier, P. L. A. *Struct. Bonding (Berlin)* **2005**, *115*, 1–56.

(11) Malcolm, N. O. J.; Popelier, P. L. A. *Faraday Discuss.* **2003**, *124*, 353–363.

(12) Popelier, P. L. A.; Aicken, F. M. *ChemPhysChem* **2003**, *4*, 824–829.

(13) Silvi, B.; Savin, A. *Nature* **1994**, *371*, 683–686.

(14) Gatti, C. Solid State Applications of QTAIM and the Source Function—Molecular Crystals, Surfaces, Host-Guest Systems and Molecular Complexes. In *The Quantum Theory of Atoms in Molecules: From Solid State to DNA and Drug Design*; Boyd, R., Matta, C., Eds.; Wiley-VCH: Weinheim, Germany, 2007; pp 165–206.

(15) Simas, A. M.; Smith, V. H.; Thakkar, A. J. *Int. J. Quantum Chem.* **1984**, S18.

(16) Bader, R. F. W.; Heard, G. L. *J. Chem. Phys.* **1999**, *111*, 8789–8798.

(17) Bader, R. F. W.; Essen, H. *J. Chem. Phys.* **1984**, *80*, 1943–1960.

(18) Carroll, M. T.; Chang, C.; Bader, R. F. W. *Mol. Phys.* **1988**, *63*, 387–405.

(19) Silvi, B. *Phys. Rev. Lett.* **1994**, *73*, 842–845.

(20) Popelier, P. L. A. *J. Phys. Chem. A* **1998**, *102*, 1873–1878.

(21) Espinosa, E.; Souhassou, M.; Lachekar, H.; Lecomte, C. *Acta Cryst. B* **1999**, *55*, 563–572.

(22) Bader, R. F. W.; MacDougall, P. J. *J. Am. Chem. Soc.* **1985**, *107*, 6788–6795.

(23) Shi, Z.; Boyd, R. J. *J. Phys. Chem.* **1991**, *95*, 4698–4701.

(24) Calvo-Losada, S.; Sánchez, J. J. Q. *J. Phys. Chem. A* **2008**, *112*, 8164–8178.

(25) Bader, R. F. W.; Popelier, P. L. A.; Chang, C. *J. Mol. Struct. (Theochem)* **1992**, *255*, 145–171.

(26) Carroll, M. T.; Cheeseman, J. R.; Osman, R.; Weinstein, H. *J. Phys. Chem.* **1989**, *93*, 5120–5123.

(27) Nekovee, M.; Foulkes, W. M.; Needs, R. J. *Phys. Rev. Lett.* **2001**, *87*, 036401.

(28) Nekovee, M.; Foulkes, W. M.; Needs, R. J. *Phys. Rev. B* **2003**, *68*, 235108.

(29) Hsing, C. R.; Chou, M. Y.; Lee, T. K. *Phys. Rev. A* **2006**, *74*, 032507.

(30) Cancio, A. C.; Chou, M. Y. *Phys. Rev. B* **2006**, *74*, 081202.

(31) Malcolm, N. O. J.; Popelier, P. L. A. *J. Phys. Chem. A* **2001**, *105*, 7638–7645.

(32) Malcolm, N. O. J.; Popelier, P. L. A. *J. Comput. Chem.* **2003**, *24*, 437–442.

(33) Popelier, P. L. A.; Burke, J.; Malcolm, N. O. J. *Int. J. Quantum Chem.* **2003**, *92*, 326–336.

(34) Malcolm, N. O. J.; Popelier, P. L. A. *J. Comput. Chem.* **2003**, *24*, 1276–1282.

(35) Keith, T. A.; Laidig, K. E.; Krug.; P.; Cheeseman.; J. R.; Bone.; R. G. A.; Biegler-König.; F. W.; Duke.; J. A.; Tang.; T.; Bader.; R. F. W. The AIMPAC95 programs, 1995, Available from: able from: http://www.chemistry.mcmaster.ca/aimpac/ (accessed Oct 14, 2010).

(36) Popelier, P. L. A. *Comput. Phys. Commun.* **1996**, *93*, 212–240.

(37) Maxwell, J. C. *A Treatise on Electricity and Magnetism*; Oxford at Clarendon Press: Oxford, U.K., 1873.

(38) Bader, R. F. W.; Essén, H. *J. Chem. Phys.* **1984**, *80*, 1943–1960.

(39) Bader, R. F. W. *J. Chem. Phys.* **1980**, *73*, 2871–2883.

(40) Bader, R. F. W.; Nguyen-Dang, T. T. *Adv. Quantum Chem.* **1981**, *14*, 63–124.

(41) Bader, R. F. W.; Preston, H. J. T. *Int. J. Quantum Chem.* **1969**, *3*, 327–347.

(42) Pendás, A. M.; Costales, A.; Luaña, V. *Phys. Rev. B* **1997**, *55*, 4275–4284.

(43) Kato, T. *Commun. Pure Applied. Math.* **1957**, *10*, 151–177.

Electron Density Laplacian

*J. Chem. Theory Comput., Vol. 6, No. 12, 2010* **3779**

(44) Desclaux, J. P. *Comput. Phys. Commun.* **1975**, *9*, 31–45.

(45) Schwarz, K.; Blaha, P.; Madsen, G. K. H. *Comput. Phys. Commun.* **2002**, *147*, 71–76.

(46) Schwarz, K.; Blaha, P. *Comput. Mater. Sci.* **2003**, *28*, 259–273.

(47) Koga, T.; Watanabe, S.; Kanayama, K.; Yasuda, R.; Thakkar, A. J. *J. Chem. Phys.* **1995**, *103*, 3000–3005.

(48) Desclaux, J. P. *Comput. Phys. Commun.* **1970**, *1*, 216–222.

(49) Blaha, P.; Schwarz, K.; Madsen, G.; Kvasnicka, D.; Luitz, J. *WIEN2k user's guide*; Techn. Universität Wien: Vienna, 2001; http://www.wien2k.at/ reg_user/textbooks (accessed Oct 14, 2010).

(50) Bader, R. F. W.; MacDougall, P. J.; Lau, C. D. H. *J. Am. Chem. Soc.* **1984**, *106*, 1594–1605.

(51) Sagar, R. P.; Simas, A. M.; Smith, V. H.; Ku, A. C. T. *J. Chem. Phys.* **1988**, *88*, 4367–4374.

(52) Shi, Z.; Boyd, R. J. *J. Chem. Phys.* **1988**, *88*, 4375–4377.

(53) Kohout, M.; Savin, A.; Preuss, H. *J. Chem. Phys.* **1991**, *95*, 1928–1942.

(54) Eickerling, G.; Reiher, M. *J. Chem. Theory Comput.* **2008**, *4*, 286–296.

(55) Becke, A. D.; Edgecombe, K. E. *J. Chem. Phys.* **1990**, *92*, 5397–5403.

(56) Tao, J.; Vignale, G.; Tokatly, I. V. *Phys. Rev. Lett.* **2008**, *100*, 206405.

(57) Biegler-König, F. W.; Bader, R. F. W.; Duke, A. J.; Nguyen-Dang, T. T.; Tal, Y. *J. Phys. B* **1981**, *14*, 2739–2751.

(58) Biegler-König, F. W.; Bader, R. F. W.; Tang, T. H. *J. Comput. Chem.* **1982**, *3*, 317–328.

(59) Cioslowski, J.; Nanayakkara, A.; Challacombe, M. *Chem. Phys. Lett.* **1993**, *203*, 137–142.

(60) Cioslowski, J.; Stefanov, B. B. *Mol. Phys.* **1995**, *84*, 707–716.

(61) Popelier, P. L. A. *Comput. Phys. Commun.* **1998**, *108*, 180–190.

(62) Sanville, E.; Kenny, S. D.; Smith, R.; Henkelman, G. *J. Comput. Chem.* **2007**, *28*, 899–908.

(63) Andersen, O. K. *Phys. Rev. B* **1975**, *12*, 3060–3083.

(64) Madsen, G. K. H.; Blaha, P.; Schwarz, K.; Sjostedt, E.; Nordstrom, L. *Phys. Rev. B* **2001**, *64*, 195134.

(65) Sjöstedt, E.; Nordström, L.; Singh, D. J. *Solid State Commun.* **2000**, *114*, 15.

(66) Brouder, C. *Phys. Rev. B* **2005**, *72*, 085118.

(67) Perdew, J. P.; Burke, S.; Ernzerhof, M. *Phys. Rev. Lett.* **1996**, *77*, 3865–3868.

(68) Otero-de-la Roza, A.; Luana, V. *Comput. Phys. Commun.* **2009**, *180*, 800–812; Source code distributed by the CPC program library. http://cpc.cs.qub.ac uk/summaries/AECM_ v1_0.html (accessed Oct 14, 2010).

(69) Otero-de-la Roza, A.; Blanco, M. A.; Martn Pendás, A.; Luaña, V. *Comput. Phys. Commun.* **2009**, *180*, 157–166; Source code distributed by the CPC program library. http://cpc.cs.qub. ac.uk/summaries/AECB_v1_0.html (accessed Oct 14, 2010).

(70) Gražulis, S.; Chategnier, D.; Downs, R. T.; Yokochi, A. F. T.; Quirós, M.; Lutterolli, L.; Manakova, E.; Butkus, J.; Moeck, P.; Le Bail, A. *J. Appl. Crystallogr.* **2009**, *42*, 726–729; http://www.crystallography.net/ (accessed Oct 14, 2010).

(71) Wyckoff, R. W. G. *Crystal Structures*; Robert E. Krieger: Malabar, 1986.

(72) Gatti, C. Private communication.

(73) Popelier, P. L. A. *Chem. Phys. Lett.* **1994**, *228*, 160–164.

(74) Rodríguez, J. I.; Koester, A. M.; Ayers, P. W.; Santos-Valle, A.; Vela, A.; Merino, G. *J. Comput. Chem.* **2009**, *30*, 1082–1092.

(75) Dovesi, R.; Saunders, V. R.; Roetti, C.; Causà, M.; Harrison, N. M.; Orlando, R.; Aprà, E. *CRYSTAL User's Manual*; Università di Torino: Turin, 1996.

(76) Orlando, R.; Dovesi, R.; Roetti, C.; Saunders, V. R. *J. Phys.: Condens. Matter* **1990**, *2*, 7769–7789.

(77) Mori-Sánchez, P.; Martn Pendás, A.; Luana, V. *J. Am. Chem. Soc.* **2002**, *124*, 14721–14723.

(78) Aray, Y.; Rodríguez, J.; Rivero, J. *J. Phys. Chem. A* **1997**, *101*, 6976–6982.

(79) Aray, Y.; Rodríguez, J.; López-Boada, R. *J. Phys. Chem. A* **1997**, *101*, 2178–2184.

(80) Aray, Y.; Rodríguez, J.; Vega, D. *J. Phys. Chem. B* **2000**, *104*, 5225–5231.

(81) Aray, Y.; Rodríguez, J.; Vega, D.; Coll, S.; Rodrguez Arias, E. N.; Rosillo, F. *J. Phys. Chem. B* **2002**, *106*, 13242–13249.

(82) Aray, Y.; Vega, D.; Rodríguez, J.; Vidal, A. B.; Grillo, M. E.; Coll, S. *J. Phys. Chem. B* **2009**, *113*, 3058–3070.

(83) Luana, V.; Mori-Sánchez, P.; Costales, A.; Blanco, M. A.; Martn Pendás, A. *J. Chem. Phys.* **2003**, *119*, 6341–6350.

(84) Pendás, A. M.; Costales, A.; Blanco, M. A.; Recio, J. M.; Luaña, V. *Phys. Rev. B.* **2000**, *62*, 13970–13978.

(85) Recio, J. M.; Franco, R.; Pendás, A. M.; Blanco, M. A.; Pueyo, L.; Pandey, R. *Phys. Rev. B* **2001**, *63*, 184101−1−7.

(86) Contreras-García, J.; Mori-Sánchez, P.; Silvi, B.; Recio, J. M. *J. Chem. Theory Comput.* **2009**, *5*, 2108–2114.